Journal of Sustainable Mining 18 (2019) 208–225

HOSTED BY

Contents lists available at ScienceDirect

Journal of Sustainable Mining

journal homepage: www.elsevier.com/locate/jsm

Research article

A scalar-geometric approach for the probable estimation of the reserve of some Pb-Zn deposits in Ameri, southeastern Nigeria

Innocent J. Arinze, Chidubem O. Emedo*, Charles C. Ugbor

Applied Geophysics Unit, Department of Geology, University of Nigeria, Nsukka, 410001, Nigeria

ARTICLE INFO

Keywords:
Ameri
Reserve estimation
Resistivity
Deposit
Vein
Profile

ABSTRACT

The Cretaceous sedimentary sequence of the Asu River Group in Ameri, southeastern Nigeria play host to lead-zinc ore deposits in irregular mineralized veins of non-uniform geometry. Two deposits (designated DEPOSIT A and DEPOSIT B) were economically assessed using an integrated approach. This was performed by employing a geometry-based classical scheme involving the mathematical relationship between the three cardinal variables of ore reserve estimation namely: surface area, thickness and density. Firstly, detailed and extensive geological mapping was carried out to establish the geological attribute of the mineral deposits. Since reserve estimation extends beyond exposed faces, spontaneous potential traverse, vertical electrical sounding and horizontal profiling, being orthogonal to the trend of the enclosing veins were used to characterize the existing sub-surface stratification and create forward models that revealed the concealed ore geometry (limiting depth, lateral extents and thickness variations). Subsequent to delineation, the depth to the top of the target ore lodes was obtained by implementing the Peter's half slope technique on self-potential curves. Thickness values of the ore bodies of interest were applied in three numerical classical integration techniques, i.e. Trapezoidal, Simpson's and Simpson's third-eight rule, for volume estimation. To overcome the non-uniqueness problem of DC resistivity data interpretation, the available drilling data was applied. Samples retrieved from each lode were subjected to mass and volume analysis using the CS200 electronic balance and water displacement technique, to determine the average density of each lode. Results from 2D subsurface resistivity sections showed the lead-zinc deposits as zones of low resistivity in a background of high resistivity. The 1D stratigraphic models reveal a mean thickness estimate of 11.85 m and 10.50 m for DEPOSITs' A and B, respectively. Sample densities correlate well with the average density of pure galena. Applying the scalar-geometric rule, a combined estimate of 10,778.95tonnes was obtained, representing a relatively economically viable quantity worthy of medium scale extraction.

1. Introduction

Reserve estimations are a capital intensive undertaking. The finance required for such a program is enormous and can be in the order of hundreds of thousands of dollars. In order to ensure profitable investment, the potential product in the subsurface must be present in adequate quantity and quality to justify a decision to invest (Rolo, Radtke, & Costa, 2017). Clearly, all monetary, technologic and personnel decisions regarding a planned extraction are based on the proper understanding of the mineral assets in-place (Sinclair & Blackwell, 2002). Thus, an accurate prediction of the location and value of in situ mineral resources must be provided with an acceptable level of confidence prior to extraction.

Generally, geology and geophysics are fundamental to the process of mineral ore evaluation (Afolabi, Olorunfemi, Olagunju, & Afolayan, 2004). Understanding the geologic attribute of an ore deposit is a necessary basis on which to develop an estimate of the reserves of an ore body. The geological setting of the mineralization define features that provide limits to target minerals, indicate possible directions of continuity, or help in constraining the extent of a target i.e. localizing the target for more detailed evaluation (Sinclair & Blackwell, 2002). Information on the rock type and structural disposition of the host geologic formation is usually obtained from surface rock exposures, trenches, and drill cores.

Geophysical techniques, particularly the electrical method, are widely known to play a vital role in mineral exploration and evaluation (Monsuro, Bayewu, & Oloruntola, 2011). Commonly used as a preliminary approach, the electrical method effectively seeks

* Corresponding author. Applied Geophysics Unit, Department of Geology, Faculty of Physical Sciences, 410001, University of Nigeria, Nsukka, Nigeria.
E-mail addresses: arinzecent@gmail.com (I.J. Arinze), chidubem.emedo.pg.80047@unn.edu.ng, ecogeogranite@gmail.com (C.O. Emedo), charles.ugbor@unn.edu.ng (C.C. Ugbor).

https://doi.org/10.1016/j.jsm.2019.07.004
Received 5 January 2019; Received in revised form 24 May 2019; Accepted 23 July 2019
Available online 26 July 2019

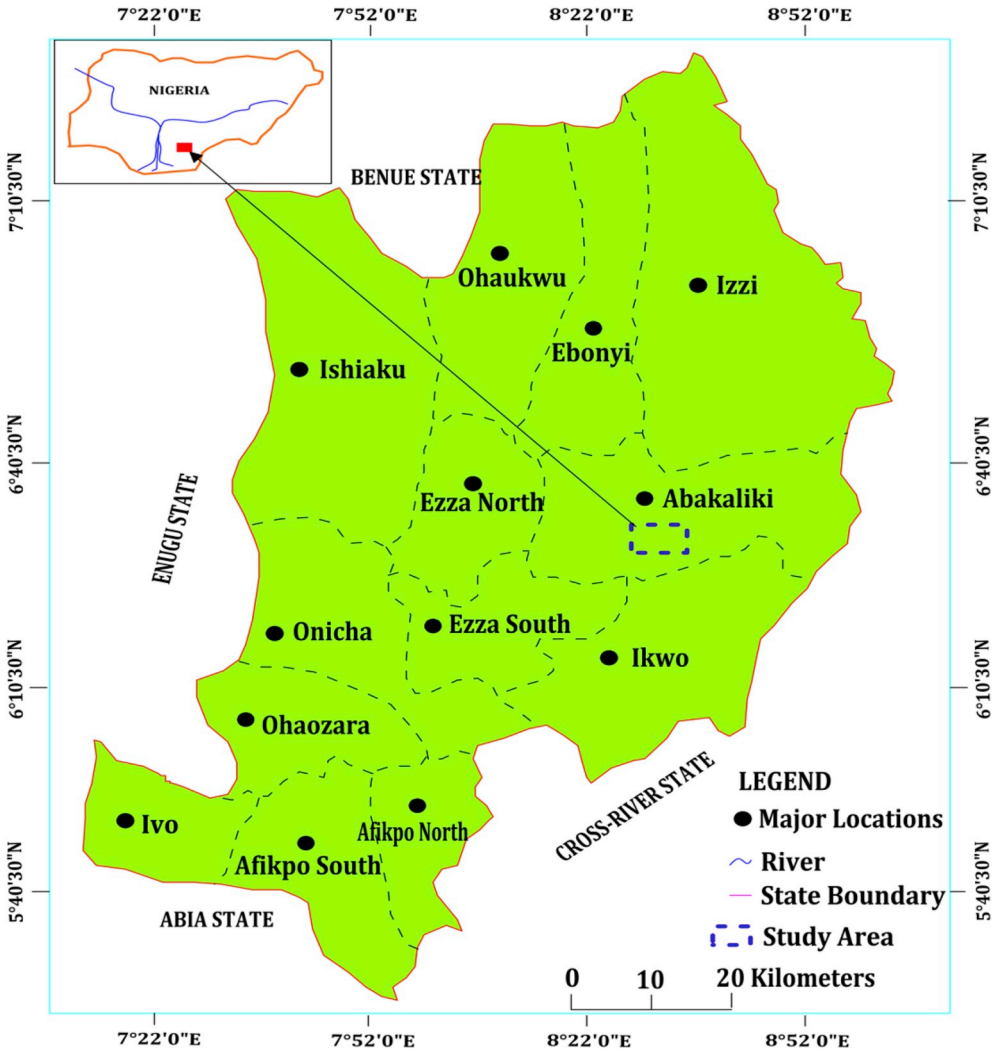

Fig. 1. Location map of the study area.

concentrations of anomalously high or low values of sub-surface resistivity/potential (Onimisi, Abaa, Obaje, & Sule, 2015). The outcome of the survey is then used to locate the mineral target of interest, or to correlate the spatial variation of recorded values of resistivity (or natural potential) with variations in the geology.

In recent years, the electrical resistivity method has benefitted from a remarkable upgrade in equipment design, as well as improved correctness of data acquisition, processing and interpretation. As a result, its application has become more widespread. Its use is not only restricted to mineral target delineation, but it is also applied during mineral tonnage assessments. This method is empirical and usually employs simple geometric rules (Wang et al., 2010). When used with close geological a-priori information, it has been proven to be quick and relatively reliable.

Despite the suitability of geophysical methods for mineral evaluation, a single technique rarely produces very reliable results. This could be attributed to a number of factors including noise, field parameters, the choice of interpretation tools and, especially, the intrinsic limitations of the method itself. Therefore, obtaining a more precise result in any geophysical survey will require a combination of two or more geophysical techniques or a validation of the results of a single technique by a more reliable process (Ramazi & Mostafaie, 2013). Generally, an integration of several methods is preferable and known to yield better results.

Several pieces of research work concerning the integration of various techniques in reserve quantification exist. Soulaimani et al. (2017) conducted a 3D modeling and reserve estimation of the Hajjar central ore body in the Marrakech region of Morocco using a combined gravity and geostatistical approach. Different parameters that defined the ore body were determined thus, enabling a 3D representation of its density distribution in the regional sub-soil. The variation rate between the 3D model and a previously generated drill model of the ore body was very minimal. Based on the result of core drilling and geostatistical interpolation, Mostafijul and Farhad (2013) investigated the reserve of a coal seam located in the northwestern part of Bangladesh. In this case, the inverse power weighing interpolation technique was applied and further compared with other estimation tools to investigate the accuracy of the calculation. The results of all the techniques showed very close agreement. Similarly, Tercan et al. (2012) carried out seam modeling and resource estimation in the coalfields of western Anatolia, Turkey. Here, a number of lignite bearing sequences were known to pose estimation problems in the past due to severe tectonic movements and highly variable coal quality. Data from statistical analysis taken from core samples of diamond drill holes was used to model fault blocks in order to establish a 3D coal seam model. The volume of the blocks was later converted into in-situ tonnages based on their estimated densities.

In Nigeria, Obi, Ekwueme & Apeke (2014), using mainly geological and geophysical means implemented a probable reserve assessment of some barite deposits hosted by Cretaceous sediments in the Cross-River

state, southeastern Nigeria. The vein-type barite bodies posted a reserve of approximately 774, 345 metric tons. In another study, Monsuro et al. (2011) integrated geophysical and geostatistical methods in the quantification of an outcropping clay deposit at Idofe, southwestern Nigeria. Despite requiring validation by drilling, the methods proved fairly reliable, efficient and cost effective.

The purpose of this study is to utilize available data obtained from geological mapping, geophysical observation, geostatistical analysis and sampling, to determine a probable reserve of lead-zinc deposits located in the Ameri mineral district, southeastern Nigeria. This work was borne out of the need to provide preliminary value assessment of mineral deposits in the study area as a solution to their limited exploitation.

Specific objectives include; producing a map of the spatial distribution of current lead-zinc mining exposures within the area, defining the linear trends of veins, delineating areas of ore occurrence as well as defining their extent of subsurface coverage and salient geometry, and, deriving an economic value prediction of selected deposits using a geometrical method.

2. Regional geological setting

The study area is located south of Abakaliki in the present day state of Ebonyi, Nigeria (Fig. 1) and lies between Latitude: 6°7′N and 6°14′N and Longitude: 8°5′E and 8°12′E encompassing an area of about 400 km^2. The area is underlain by the low-lying Abakaliki Formation which is a part of the Benue Trough of Nigeria and a major geological feature in Africa that stretches over 1000 km from its southeastern section to Bauchi State in the northeastern region of Nigeria (Fig. 2). The formation of the trough is connected to the regional tectonic event that resulted in the separation of the African and South American continents in the early Cretaceous period (Farrington, 1952). It is regarded as a part of the Pan African Mobile Zone of West Africa and considered a NE-SW elongated trough of subsidence (Fig. 3a).

The Benue Trough is arbitrarily segmented into three sections, from southwest to northeast; the Lower, Middle and Upper Benue Trough (Maurin, Benkelil & Robineau, 1986). The lead-zinc fields occur in the Benue Trough, in a narrow belt that stretches over 560 km from Ishiagu in the southeast through to Azara in the middle belt to Gidan Dari in the Upper Benue Trough (Fatoye, Ibitomi, & Omada, 2014). The Abakaliki Formation forms a part of the lower section of the trough.

Three cycles of basin deposition have been reported in the lower Benue Trough: the marine Neocomian-Albian Asu River Group, the Turonian Eze-Aku Group and the Coniancian-Santonian Awgu Group. Sediments of the Abakaliki Formation which is a member of the Asu River Group (Fig. 3b) underlie the study area. They consist of thick sequences of slightly deformed Cretaceous sedimentary rocks made up of essentially Albian shales with its subordinate of sandstones, siltstones and mudstones. These geological units are interpreted as sediments of the first transgressive cycle into the Benue Trough that occupy the core of the Abakaliki Anticlinorium.

Overlying the Asu River Group is the Turonian Eze-Aku Group made up of calcareous sandstones, shales and limestones. More often than not, the sandstone and limestone unit alternate with the calcareous shales. The type locality of the main shale component is located along the Eze-Aku River in the southern part of the trough (Ojoh, 1992). In the Amaseri and Ugep areas, the sandstone member of this group forms the NE-SW trending ridges that are commonly referred to as Amaseri Sandstone/Formation (Fig. 3b). These ridges, which are intensely bioturbated, are tall with a height of approximately 5 m.

The Awgu Group rests unconformably on the Eze-Aku Group and comprises the Awgu Shale and the Agbani Sandstone. Reyment (1965) reported that the Agbani Sandstone is a time-equivalent of the Awgu shale. Large scale planar and trough cross-stratification as well as herring-bone cross-beds are primary sedimentary structures that are commonly observed in the Agbani Sandstone.

Basin formation in this lower section of the trough was later influenced by two tectonic episodes; the Aptian-Cenomanian and the Albian-Santonian tectonic events (Simpson, 1954). Previous pieces of work posit that the sediments of the Abakaliki Formation were affected by a minor folding event during the Cenomanian period and a more intense folding phase, accompanied by igneous intrusions during the Santonian period. The intensive magmatism and subsequent Santonian deformation displaced the major depositional axis in the westward direction and led to the formation of the Anambra Basin (Fatoye et al., 2014).

Structural features within the trough are mostly represented by

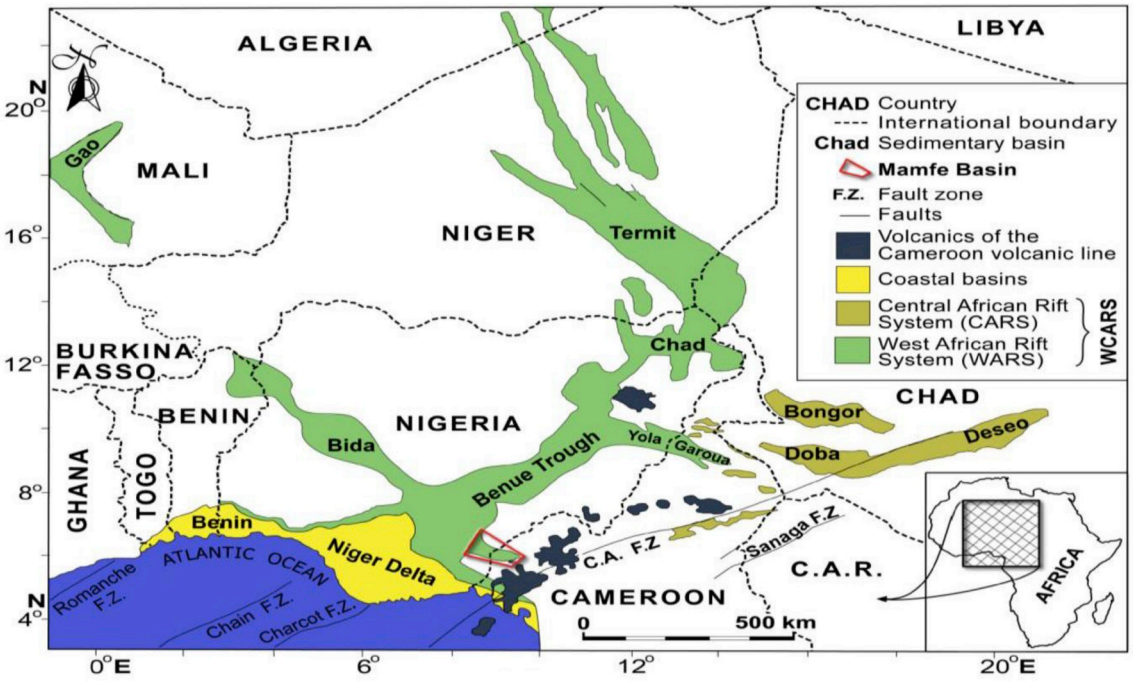

Fig. 2. Map of the Central and West African rift systems (WCARS) (modified after Genik, 1993).

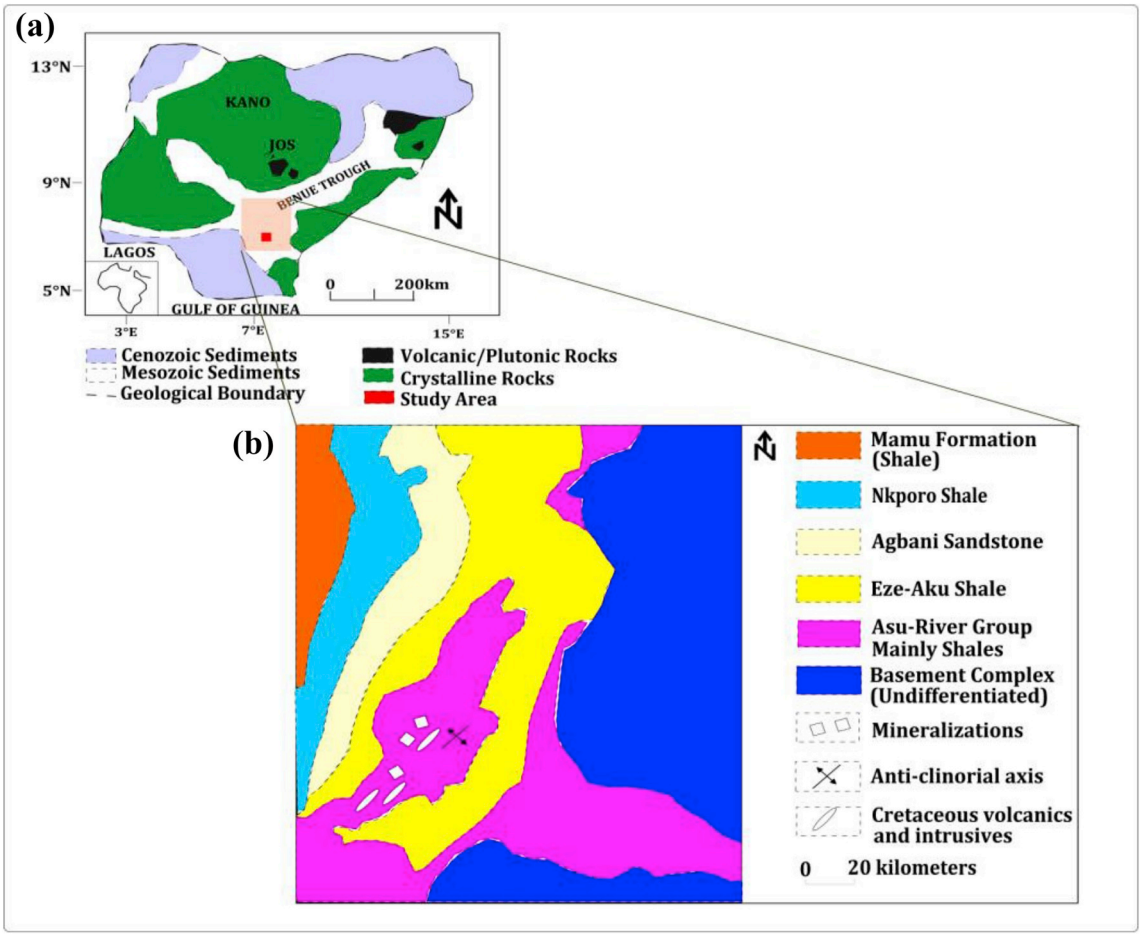

Fig. 3. (a) Generalized Geology of Nigeria showing the location of the Benue Trough and study area (modified after Olade, 1976). (b) Geology of lower Benue Trough in and around the study area (modified after Hoque, 1984).

folds produced during the Santonian tectonic deformation (Farrington, 1952; Orajaka, 1965; Nwachukwu, 1972; Offodile, 1976; Maurin & Lancelot, 1987; Leach et al., 2010; Oha, Mosto, & Dada, 2017). In the lower Benue Trough, where Ameri is located, intensive compressional folding produced the Abakaliki Anticlinorium with other minor synclines and anticlines (Murat, 1970). Fracture development in these Cretaceous sedimentary rocks depends on the physical characteristics and competence of the individual rock types. Abundant development of gangue and ore minerals in partially filled disconnected irregular-shaped pores and elongated vesicles within the shaley bedrock have been observed (Grant, 1971; Nwachukwu, 1975; Offodile, 1976; Offodile & Reyment, 1976, pp. 37–66; Olade, 1976; Olade & Morton, 1985; Maurin, 1986, p. 211; Maurin & Lancelot, 1987 and Etim, Louis, & Maurin, 1988). The sediments are folded, mainly, along E-W directions with the anti-clinal axis trending in the NE-SW directions (Fig. 3b) (Akande & Mucke, 1989; Ezepue, 1984; Obasi, Gundu, Ashwe, & Akindele, 2015). Fractures and faults occur in diagonal parallel rows and strike N-S with vertical dips.

3. Materials and methods

3.1. Geological mapping

Field and analytical approaches were adopted. In the field, extensive geological mapping was undertaken as a fundamental precondition to ore reserve inventory with special emphasis on linear trends. The aim is to unravel the structural disposition of the ore deposits within the underlying geological formation, as well as to visually determine the mineralogical composition of the ores around the areas of mineralization. The results of geologic field mapping were used to produce a geologic map that revealed the spatial distribution of current lead-zinc mineralized sites in the study area.

3.2. Geophysical detection

Self-potential traversing, horizontal profiling (HRP) and vertical sounding (VES) schemes were all employed in subsurface geophysical detection. These profile lines were run in order to capture the subsurface geological structures and identify mineral ore bodies based on the striking differences between resistivity/natural potential values and their relation to the known geological features in the study area. During the HRP survey, lateral sub-surface mapping was carried out from five parallel lines of electrical tomography using the ABEM SAS 1000 terrameter, which employed a standard four electrode Wenner spread (Fig. 4a). 50 m spacings were kept between the traverse lines. The orientation of these profiles was based on prior structural assessment, planned to be orthogonal to the predominant linear direction. Horizontal profiling is used to investigate lateral changes in apparent resistivity that reflects lateral geological variability or localized anomalous features. For such investigations, the apparent resistivity at each measurement location for the Wenner configuration is obtained using the expression:

$$\rho_a = \frac{\Delta V 2\pi}{I} a \quad (1)$$

Where, ρ_a = apparent resistivity, Δv = potential difference, I = inputed current. a is the fixed current and potential electrode spacing (Fig. 4a).

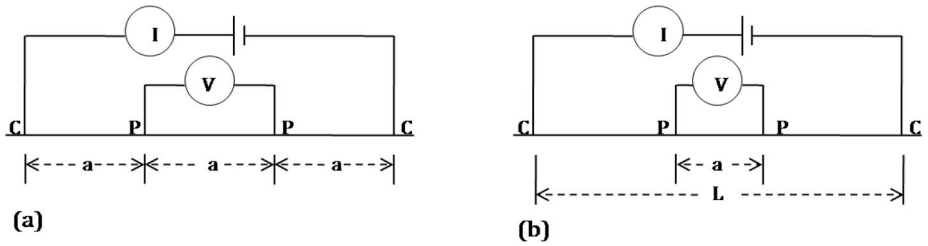

Fig. 4. a. Wenner electrode configuration b. Schlumberger electrode configuration (C = current electrode and P = potential electrode).

Four electrodes are placed in steps along a traverse while maintaining constant values of the inter-electrode separations in line with the Wenner configuration. The separation of the current electrodes is chosen so that the current flow is maximized in depths where lateral resistivity contrasts are expected. The survey reveals horizontal variations in resistivity within an area at a particular depth (Lowrie, 2007).

The resistivity contrast between the ore body and host rock is often large, because the resistivities of different rocks and minerals vary widely. Anomalies were detected by the high conductivity (low resistivity) of the mineral bodies present in rocks of higher resistivity.

The acquired data was subjected to 2D inversion using Res2dinv software to generate 2D subsurface resistivity sections. These resistivity tomography sections are commonly presented as resistivity pseudosections that give a near-precise resemblance of sub-surface resistivity distribution. They define the lateral extent of subsurface geological structures.

While numerous modeling techniques such as fuzzy modeling based on spatial variability, fractal modeling, modeling based on Artificial Neural Network and modeling using support vector machine exist, this study employed variogram based modeling to provide a quantitative description of natural variables (resistivity in this case) distributed in space. It considers the spatial correlation between data, including distance and direction and can be expressed in arithmetical form which considers the spatial structure. In this work, the spatial structure of the resistivity around the survey area was modeled geostatistically by means of a variogram. The purpose was to aid the easy identification of areas of possible mineral occurrence based on the distribution of the resistivity values (Ramazi & Mostafaie, 2013).

To achieve this, a spherical variogram with a nugget of 1.5, range of 1020, and sill of 75 was fit to the existing data using the variogram fitting interface in the Stanford Geostatistical Modeling Software (SGeMS). A 200 m by 300 m grid of 10 m by 10 m cells was defined in SGeMS. The grid was loaded as well as the data points and ordinary kringing was run using variogram. This generated a resistivity field that revealed the spatial structure of resistivity distribution within the survey area.

The VES technique, due to its superior vertical coverage was adapted using the Schlumberger configuration (Fig. 4b) to determine the variation of apparent resistivity with depth (Odeyemi, Oloruniwo, & Folami, 1997). Two pairs of electrodes made of steel were driven into the ground at each end of the spread. The transmitter pair was connected to the current sender (Terrameter), located in the center, by two 16-gauge cables. The potential pair, which was also driven into the earth, was connected to the voltage receiver, in the center. The electro-potential distance was kept constant for each set of readings while the current pair was progressively expanded around the fixed center (Loke & Barker, 1996). The value at each measurement point was derived by applying the apparent resistivity equation corresponding to the Schlumberger electrode array, as below:

$$\rho_a = \frac{\pi}{4}\frac{\Delta V}{I}\left(\frac{L^2 - a^2}{a}\right) \quad (2)$$

Where, ρ_a = apparent resistivity, Δv = potential difference, I = input current. 'L' is the large current separation and a, the electro-potential distance (Fig. 4b).

The purpose of this was to observe the variation of resistivity with depth. In this case, the mid-point of the array is kept fixed while the distance between the current electrodes is progressively increased. This causes the current lines to penetrate to greater depths, depending on the vertical distribution of conductivity (Lowrie, 2007).

The collected data was modeled in 1D using WinResist iterative software, and interpreted quantitatively to determine the nature of the underlying geological formations, presented with its possible geological meanings, resistivity values and layer thicknesses. The purpose of these resistivity transects is to provide the quantitative value of the thickness variations of the Pb-Zn bodies beneath the VES points.

Additionally, self-potential profiles were run separately but along the same traverse and direction as other electrical profiles. For the natural potential to be generated, the ore body is expected to straddle the water table. Since the ground above the water table is more accessible to oxygen than the submersed part and since the moisture above the water table contains more oxidized ions than that below it, an electrochemical reaction takes place at the surface between the ore body and the host rock above the water table. This results in the reduction of the oxidized ions in the adjacent solution causing an excess of negative ions to appear above the water table. At the same time, a simultaneous reaction between the submersed part of the ore body and the groundwater results in oxidation of the reduced ions present in the groundwater thereby producing excess positive ions in the solution and liberating electrons at the surface of the ore body, which acts as a conductor that connects the two half-cells. Electrons flow from the deep part to the shallow part of the ore body. Outside the ore body, positive ions move from bottom to top along the electric field lines. The equipotential surfaces are normal to the field lines. The self-potential is then measured where they intersect the ground surface (Lowrie, 2007).

Self-potential (SP) anomalies across ore bodies are invariably negative, usually amounting to a few hundred millivolts. They are most commonly associated with sulfide ores, such as galena, sphalerite, pyrite pyrrhotite, and chalcopyrite.

The field instrument used comprises simply of a pair of electrodes connected via a sensitive high impedance milli-voltmeter to measure the natural potential difference between the two electrodes which are implanted in the earth. Ordinary metal stakes were inadequate as electrodes, because electrochemical reactions take place between the metal and the moisture in the earth, causing the build-up of spurious charges on the electrodes, which can falsify or obscure the small natural spontaneous-potentials. To ameliorate this effect non-polarizable electrodes were utilized. Three traverses were performed by implanting one electrode in barren ground and moving the other over the survey area. Station spacing was 20 m. With this method the total potential was measured directly at each station. The wire connecting the electrodes was long enough to allow good coverage of the area of interest resulting in smaller cumulative error. This enables more flexibility when placing the mobile electrode and usually provides data of better quality.

The acquired data was copied into Microsoft Excel sheet to generate line graphs which were used in the manual computation of depth by employing the Peter's half width method. This method is a graphical based approach applied in the estimation of depth to the top of an ore body. The implementation of this technique requires careful

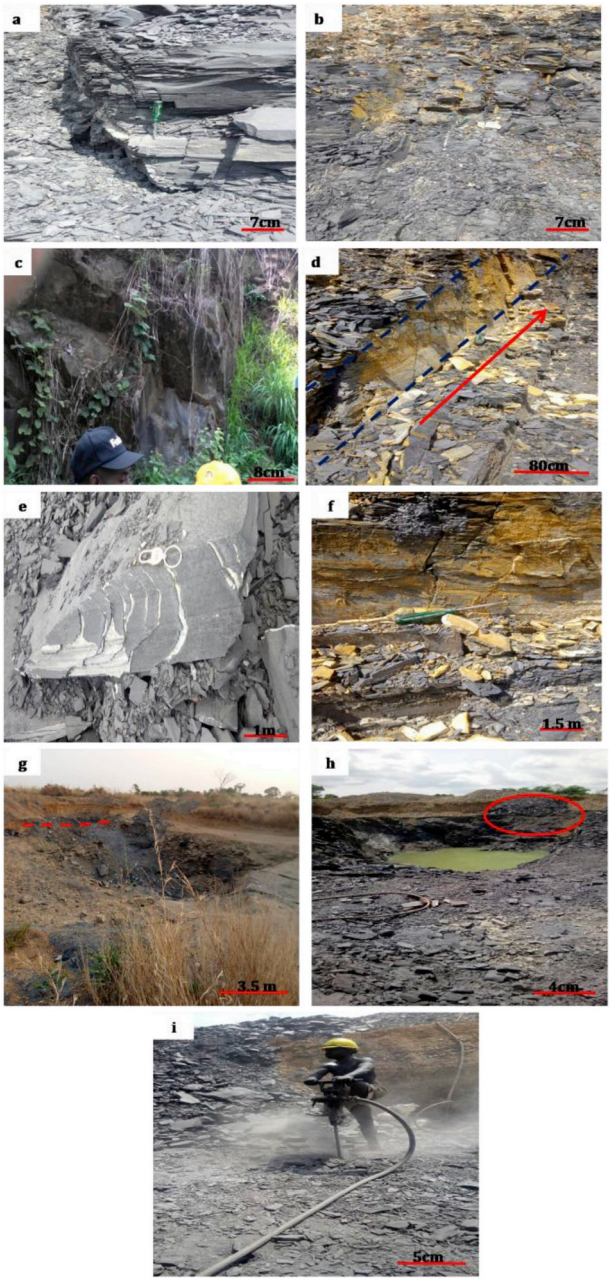

Fig. 5. (a) Photograph of baked shales of the Asu River Group. (b) Highly fractured baked shales. (c) A concordant igneous sill located far away from the vicinity of the ore deposits. (d) NW-SE trending vein indicated by the arrow direction (the broken line shows the width of the vein to be approximately 40 cm). (e) Quartz gangue mineral at a mine site. (f) Iron sulphide minerals lining the side of a vein. (g) Broken line showing the contact between overburden and shale. (h) Abandoned mine site at Ameri (the red circle indicates the mine tailings). (i) Pre-blasting drilling operation at a mine. (For interpretation of the references to colour in this figure legend, the reader is referred to the web version of this article.)

identification of the anomaly maxima and minima on the slope of a self-potential anomaly line graph. Afterwards, two parallel lines are drawn to form tangents at the anomaly maxima and minima. The horizontal distance between these two tangents is denoted as *d*. Depending on the perceived size of the causative body, a proportionality index is assigned and the depth to the top of the ore body is ascertained by dividing the horizontal length by the index value (Adegoke & Layade, 2014). For the purpose of this study, an index value of 0.83 is applied implying that the depth to the top of the ore deposits given by:

$$H = 0.83d \tag{3}$$

3.3. Volume estimation

After extracting the spatial and thickness data from the sounding curves, grid files were automatically produced. Subsequently, volume evaluation was implemented for each cell by using different approaches of interpolation and integration.

Volume computations are accomplished in ore bodies defined by an upper and lower surface. The upper and lower surfaces are delineated by a grid file or a plane of constant Z level. Blanked regions on either the lower or the upper surface are excluded from consideration during volume computations. Calculations are usually generated for each grid cell. In areas where the surface is tilted at the top or bottom of a grid cell, Surfer software approximates the volume of the prism at the bottom or top of the grid cell column. For very coarse grids, the prisms can contain significant volume. Volume calculations become more accurate as the density of the grid increases (Mostafijul & Farhad, 2013).

Arithmetically, the volume under a function $f(x,y)$ is defined by a double integral,

$$\text{Volume} = \int_{X\min}^{X\max}\int_{Y\min}^{Y\max} f(x,y)d_x d_y \tag{4}$$

In Surfer, this is calculated by first integrating over X (the columns) to obtain the areas under each row, and then integrating over Y (the rows) to get the final volume (Mostafijul & Farhad, 2013). It approximates the necessary one-dimensional integrals using three classical numerical integration algorithms: Trapezoidal Rule, Simpson's Rule, and Simpson's 3/8 Rule. The disparity in the estimations of volume by the three distinct methods indicates the accuracy of the volume calculations. If the three volume calculations are reasonably close together, the true volume is close to these values. The yield volume is usually given in cubic metres.

To validate the results of geophysical observations and, hence, overcome the non-uniqueness problem of geophysical data interpretation, drill hole data from eight vertical holes, bored with the aid of an XY200C Hydraulic Rotary drilling rig was acquired and analyzed.

3.4. Density analysis

Eight samples of Pb-Zn were collected in total, four from each lode body under evaluation. The sample points were spatially distributed within the mass of the ore bodies. A CS-200 electronic weighing balance of 0.1 g precision was used to measure the mass of each cleaned and dried sample with minimum interference from wind. Tongs were used to grip each sample before placing it on the weighing container to prevent sample contamination. Before each measurement, the scale of the balance was re-zeroed and the weighing boat completely wiped clean.

The well-known fluid-displacement technique was employed in the volume determination of the samples. In this case, water was used as the reference liquid. The procedure involved completely immersing each sample into a graduated measuring cylinder containing water of a known volume. The water level before and after the immersion of each sample was duly noted and the difference recorded. Each result indicates the measurement of the volume of displaced water which is equivalent to the volume of the sample itself. Subsequently, the mass of each sample is divided by its volume to obtain the density.

3.5. Reserve estimation

The aforementioned data, in conjunction with the results obtained from geophysical detection and geostatistical analysis, was used to derive the probable reserve of two lead-zinc deposits within the study

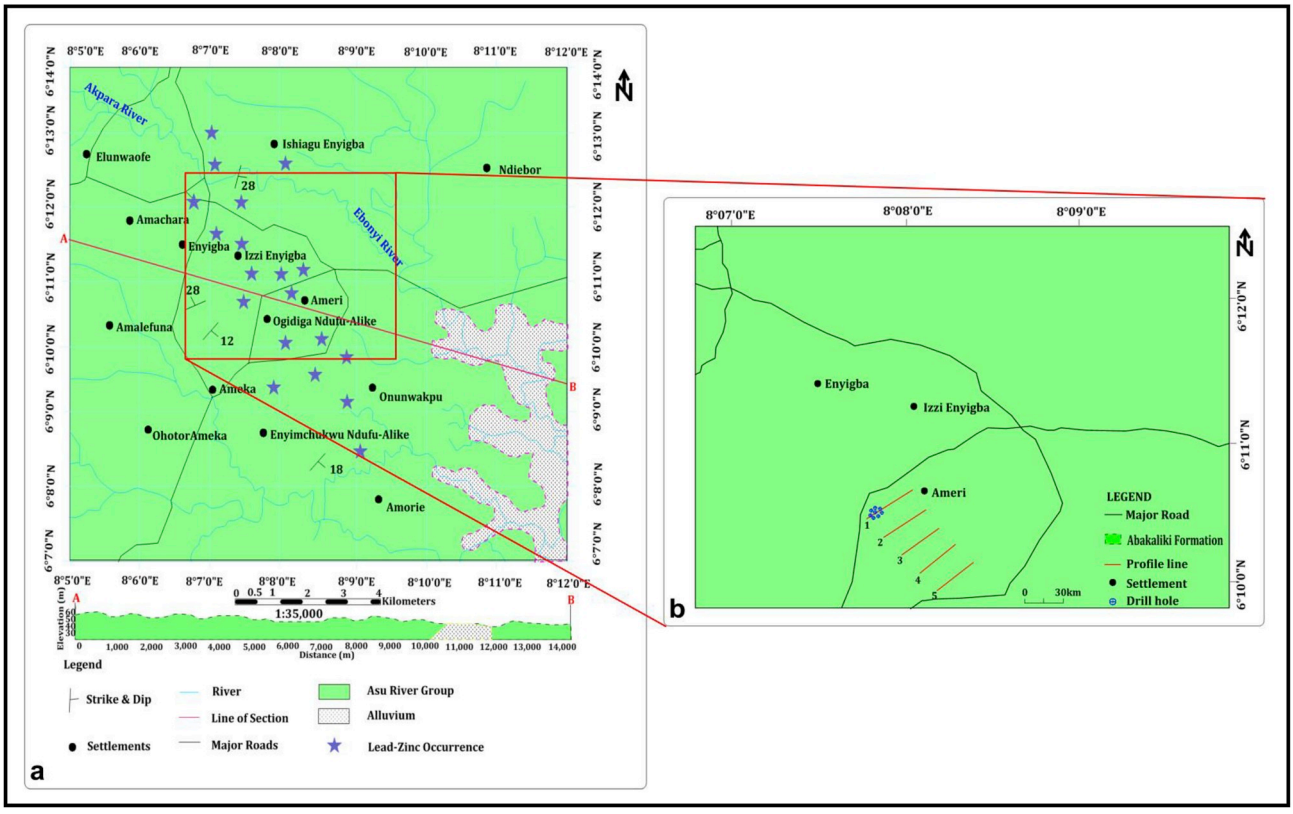

Fig. 6. (a) Geologic map of the study area showing lead-zinc deposits in a geospatial framework. (b) Abridged form of Fig. 6a around Ameri showing the profile lines and drill holes mounted atop DEPOSIT A.

area using the classical method. The reserve of each deposit was numerically estimated by applying a scalar-geometric approach involving the arithmetical relationship between the reserve, thickness, area and density of ore deposits as shown below:

Reserve estimation of a lead-zinc deposit = thickness of the Pb-Zn deposit (m) × area of the Pb- Zn deposit (m^2) × density of the Pb-Zn deposit (kg m^{-3}). (5)

The estimated total reserve of both deposits was determined by summing the reserves of the individual deposits.

4. Results and discussion

4.1. Ore geology

The dispersal of current Pb-Zn mineralized sites around the study location show a slightly definite trend, which is approximately NW-SE and perpendicular to the major axis of the basin. The host formation is the Albian shales of the Asu River Group (Fig. 5a). These shales with their subordinate sandstones, siltstones and clay are baked in some areas (Fig. 5b). Mineral ores are spatially related with igneous rocks and brine springs although these igneous bodies are conspicuously absent in the immediate vicinity of the mineral bodies (Fig. 5c). The widespread spatial associations between the mineralized veins and basic intrusive bodies around the study area may have some genetic indications.

Indications from geological field work also suggest that mineralization is structurally controlled and restricted to the less prominent and parallel NW-SE trending fractures. Vein widths range from a few centimeters to tens of meters and from tens of centimeters to over 1500 m in length (Fig. 5d). The wide variation in the size of the mineralized veins could be attributed to the slightly heterogeneous nature of the geological formation. There is less variation in the ore within the study area where there is a noticeable dominance of galena and sphalerite within the ore bodies. These minerals are frequently associated with quartz, copper and iron minerals (pyrite, chalcopyrite, marcassite, and siderite) as gangue sometimes occurring in the form of veins and veinlets associated with the host rocks (Fig. 5e and f). This gangue minerals make-up about 2–3% of the ore body and the gangue model of lead-zinc mineralization genesis has been reported to contain quartz, calcite, siderite, marcassite, pyrite, and chalcopyrite in the shale host rocks.

Furthermore, fracturing and jointing are intense in the areas of mineralization. The deposits in this area seem to show lithologic affinity with shale constituting the host rock. They mainly occur as lead-grey crystalline materials with cubic cleavage. The well crystallized cubic structure is generally sheared and consists of parallel strips of contrasting colors commonly known as striations. The cubic form was probably deposited prior to or contemporaneously with the deformation event that affected the host rocks in Cenomanian times (Nwachukwu, 1972).

Two bodies of lead-zinc exposures designated as DEPOSIT A and DEPOSIT B were identified for quantitative evaluation. DEPOSIT A is located at Latitude 6°10′35.69″N and Longitude 8°7′50.63″E and trends in a NE-SW direction. It predominantly consists of galena and sphalerite in host rocks of black carbonaceous shales of the Asu River Group (Fig. 6a and b) with bands of ferrogenized sandstone. Siderite, chalcopyrite and quartz occur as major gangue minerals. DEPOSIT B, which is approximately 0.49 km from DEPOSIT A on a NW-SE axis is located at Latitude 6°10′53.56″N and Longitude 8°7′34.69″E. In this deposit, galena which had a characteristic cubic cleavage similar to those observed in DEPOSIT A, ranks second to sphalerite in relative abundance. Here, quartz minerals occur as crystalline white substances that coat the earlier deposited sphalerite. Both deposits exhibit sharp contact with the surrounding host rock.

Table 1
Resistivity data for Profile 1 and Profile 2.

Elect. spacing (m)	Profile 1	Standard deviation	Profile 2	Standard deviation	Elect. spacing (m)	Profile 1	Standard deviation	Profile 2	Standard deviation
	Apparent resistivity (Ωm)		Apparent resistivity (Ωm)			Apparent resistivity (Ωm)		Apparent resistivity (Ωm)	
10	133.14	0.019	117.90	0.251	30	178.42	1.257	56.79	2.176
10	131.94	0.023	87.41	0.337	30	161.46	0.060	79.69	0.135
10	76.36	0.045	179.98	0.010	30	825.76	0.196	364.48	0.067
10	83.32	0.011	71.76	0.097	30	490.39	0.035	787.76	0.168
10	348.10	0.037	106.87	0.125	30	425.77	0.022	195.12	0.124
10	68.87	0.095	87.93	2.135	30	170.39	0.134	96.62	0.156
10	90.43	0.146	144.33	1.002	30	150.82	0.094	426.51	0.624
10	992.80	0.243	67.63	1.654	30	203.80	0.032	458.55	0.832
10	99.79	0.762	145.85	0.002	30	523.10	0.138	109.63	0.084
10	297.50	1.269	514.81	2.156	30	129.40	0.114	539.76	0.157
10	118.27	2.435	93.06	0.194	30	729.84	0.127	332.75	0.156
10	101.59	0.066	131.26	0.167	40	884.10	0.562	816.79	0.016
10	200.68	3.251	131.14	0.132	40	476.56	0.006	345.78	0.921
10	119.78	2.478	91.39	0.176	40	583.76	0.197	253.58	0.792
10	558.99	0.073	875.38	0.432	40	181.20	1.233	608.39	0.336
10	200.50	1.675	162.62	0.145	40	424.76	1.056	362.28	0.127
10	77.93	0.100	68.95	0.143	40	187.41	1.117	378.23	0.421
10	519.86	4.753	68.45	0.177	40	220.73	1.804	291.78	0.046
10	173.74	1.764	443.55	0.128	40	91.44	0.192	114.32	0.017
10	920.69	2.424	70.34	0.143	40	244.43	0.142	250.32	0.162
20	281.37	8.114	820.01	0.111	40	223.20	0.552	798.74	0.715
20	85.12	2.015	653.05	0.215	40	654.95	0.538	247.93	0.051
20	265.84	5.130	681.52	0.942	50	157.97	0.142	87.47	0.153
20	200.91	0.023	578.01	0.154	50	373.00	0.029	604.10	0.112
20	205.45	0.153	675.20	0.137	50	142.70	0.115	152.80	0.212
20	620.39	0.326	86.26	0.132	50	400.70	0.423	71.25	0.091
20	765.98	0.013	82.29	0.967	50	562.19	0.361	502.03	0.352
20	189.10	2.541	862.17	0.541	50	127.71	0.451	625.09	0.002
20	124.14	0.016	851.95	0.882	50	293.73	0.057	382.20	0.521
20	88.92	3.671	69.29	0.143	50	249.36	0.135	372.49	0.662
20	672.00	2.051	88.69	0.315	60	249.28	0.126	968.56	0.216
20	163.40	4.228	90.02	0.167	60	74.16	0.132	384.19	0.771
20	453.50	0.013	198.88	0.972	60	717.37	0.221	444.01	0.005
20	151.27	0.043	518.37	0.021	60	277.95	0.019	578.91	0.162
20	96.10	0.194	64.59	0.065	60	480.28	0.193	787.45	0.414
20	86.80	0.126	104.39	0.194	70	402.86	0.626	122.57	0.009
20	807.20	0.137	176.81	0.631	70	809.99	0.127	982.55	0.145
30	670.80	0.154	119.99	0.056	–	–	–	–	–
30	149.60	0.132	71.92	0.087	–	–	–	–	–
30	84.968	0.188	832.38	0.111	–	–	–	–	–

4.2. Characterization of the deposits from 2D tomographic sections

The apparent resistivity data recorded for two horizontal profile lines (Profile 1 and 2) is shown in Table 1 and the corresponding inverted 2D model sections exported from Res2dinv are presented in Figs. 7a and 8.

In profile 1, the occurrence of Pb-Zn mineralization is represented by blue color and is characterized by low resistivity values that vary between 68.87 and 99.79 Ωm, observed at surface positions, 20–50 m and 95–135 m along the traverse line where it intersects with a slaty background of high resistivity that ranges from 453.50 to 992.80 Ωm (Fig. 7a). Areas of intermediate resistivity are suggestive of unsaturated sandstone.

Although two bodies of Pb-Zn deposits were observed in this profile, the target ore body for evaluation is the lode revealed from 20 to 50 m along the profile line herein referred to as DEPOSIT A. The limiting depth of this deposit inferred from the profile is about 5.2 m from the ground surface where it extends vertically to a depth of about 25.6 m.

The 2D inverse resistivity model structure of profile 2 shows a number of smaller deposits of Pb-Zn disseminated at various points and encountered at surface locations of 15 m, 40 m, 80 m, 120 m and 200 m, along the profile (Fig. 8). The tectonic deformational events that occurred in the study area's geological history gave rise to the spatial disposition of these lode bodies.

The resistivity data obtained for Profiles 3 and 4, which traversed a direction orthogonal to the orientation of the mineralized veins, is presented in Table 2 and their respective pseudosections of resistivity in terms of distance and depth are shown in Figs. 9 and 10.

In Fig. 9, three resistivity signatures are apparent along the profile (Profile 3). Resistivity imaging values as low as 14.99–90.99 Ωm allows the setting of a geophysical signature of low resistivity interpreted as bodies of Pb-Zn deposits seated in a shaley host rock of higher resistivity that ranges from 568.36 to 79.90 Ωm, representing the second resistivity structure. The third resistivity structure is interpreted lithologically as unsaturated sandstones and siltstones with intermediate resistivity values in the range of 110.50–489.10 Ωm.

In Fig. 10a (Profile 4), shallower prospects occur as disconnected deposits distributed at different points along the profile line. Similar signatures are also observed in Profile 5, although in Profile 4, the section shows the existence of a deeply seated lode positioned with the center in 75 m of the line, which has a higher dimension than the shallower deposits previously identified. While five masses of Pb-Zn deposits were delineated in this profile, economic assessment was determined on the deposit revealed between 40 and 55 m along the traverse. This lode is referred to as DEPOSIT B (Fig. 10b). Table 3 shows the apparent resistivity data obtained for Profile 5.

The lateral extents of DEPOSITs' A and B inferred from the pseudosections of resistivity are 30 m and 20 m respectively (Figs. 7a and

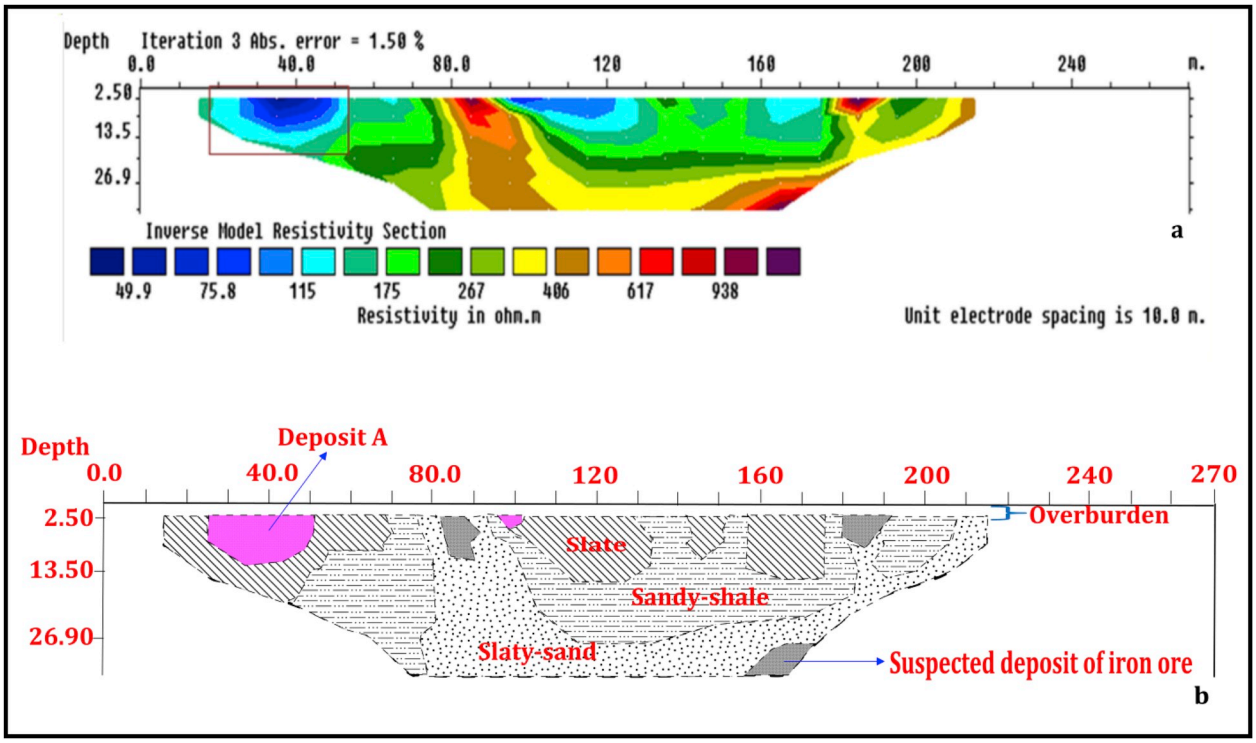

Fig. 7. (a) Sub-surface model of resistivity distribution along Profile 1. Blue areas represent zones of low resistivity and indicate Pb-Zn deposits. DEPOSIT A is enclosed in a square box. (b) Lithologic interpretation of Profile 1. The colors in Fig. 7a are assigned geological meanings (For interpretation of the references to colour in this figure legend, the reader is referred to the web version of this article).

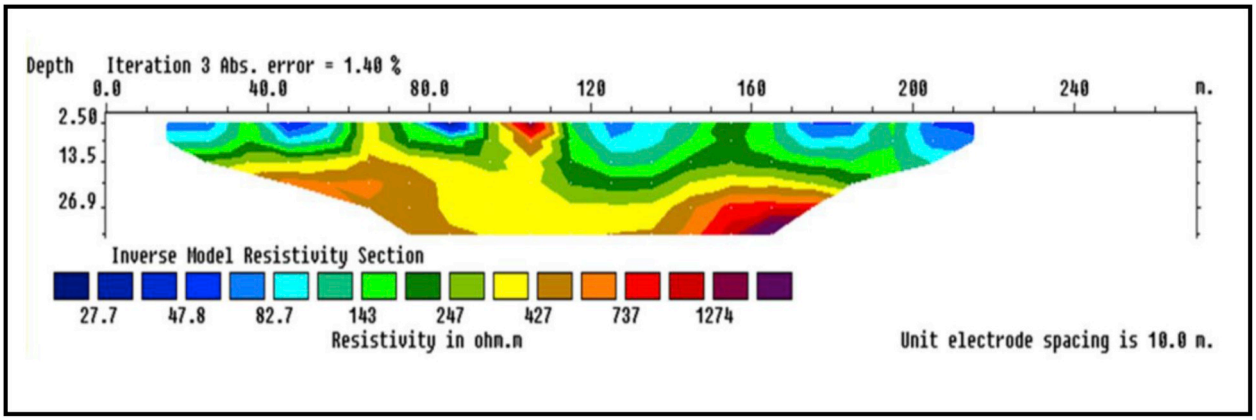

Fig. 8. Sub-surface model of resistivity distribution along Profile 2.

10a). This implies that DEPOSIT A is of greater length than DEPOSIT B. The width of the housing veins may have influenced the size and, therefore, the surface areas of these deposits.

Additionally, the section (Profile 1) reveals the maximum depth of DEPOSIT A as 13.5 m, 6.74 m greater than that of DEPOSIT B. Visually, both deposits appear to be non-complex and do not show significant variation in thickness. The use of a simple geometric approach in evaluating their reserves is considered appropriate.

To better understand the distribution of apparent resistivity with depth across the five profiles, resistivity slice maps for a = 10, 20, 30, 40, 50, 60 and 70 (a being the fixed spacing between adjacent electrodes) data points, equivalent to depths of approximately 4 m, 7 m, 10 m, 13 m, 16 m, 20 m and 24 m, respectively, were plotted and stacked (Fig. 12). The predominantly low resistivity values observed for a = 10 slice indicates weathered topsoil, a typical characteristic of sand-clay heterolith. Beneath this slice at a = 20, is a background of highly resistive shale flanked at the northwest and southeastern corners by less resistive zones that are typical of metallic mineral deposits. Below this unit, at a depth of approximately 10 m, Deposits' A and B were discerned with relatively low resistivity at the northwest and central sections respectively. At about 13 m directly beneath DEPOSIT B is a deep seated lode whose vertical extent appears to terminate at 16 m. The low resistivity signature observed below this depth is attributed to sand-clay lithology.

Data acquired from electrical resistivity imaging was inputted into the Stanford Geostatistical Modeling Software (SGeMS) tool to generate a variogram based block model displayed in Fig. 13. The model reveals the resistivity structure around the survey area.

In the plan view, the periphery (edge) of the model reveals high resistivity zone with values that vary from 956.5 to 1145 Ωm depicting the dry overburden rock unit (Fig. 13). At the top, the central portion of the model shows intermediate resistivity values ranging from 578.6 to 767.6 Ωm and corresponds to the resistivity of the shale host rock. The shale signature observed at the surface of the model is an indication of a

Table 2
Resistivity data for Profile 3 and Profile 4.

Elect. spacing (m)	Profile 3	Standard deviation	Profile 4	Standard deviation	Elect. Spacing (m)	Profile 3	Standard deviation	Profile 4	Standard deviation
	Apparent resistivity (Ωm)		Apparent resistivity (Ωm)			Apparent resistivity (Ωm)		Apparent resistivity (Ωm)	
10	109.30	0.125	80.10	2.765	30	587.81	1.674	151.88	1.267
10	88.60	0.076	69.30	0.016	30	84.70	1.065	776.30	2.113
10	103.60	0.146	110.90	1.356	30	435.10	0.976	826.32	0.986
10	97.34	0.153	78.86	1.226	30	378.66	0.236	620.10	0.123
10	979.90	0.176	74.65	1.752	30	815.78	1.763	87.369	7.183
10	84.15	0.923	734.60	1.846	30	80.68	1.653	119.63	0.127
10	778.99	0.885	167.50	0.003	30	87.61	1.892	270.36	2.367
10	468.20	0.153	207.22	2.674	30	485.11	1.769	202.10	2.663
10	685.60	0.021	91.50	8.115	30	799.08	0.003	177.29	0.194
10	123.70	0.032	450.40	2.176	30	728.10	2.451	274.10	0.175
10	118.90	0.145	154.60	0.028	30	238.90	6.221	325.90	0.236
10	155.11	0.345	979.40	0.137	40	14.99	1.743	146.50	0.521
10	103.90	0.547	66.98	0.122	40	161.83	1.443	876.22	0.627
10	105.90	0.327	150.50	0.116	40	587.81	1.414	215.50	0.318
10	890.13	1.528	67.20	0.762	40	883.10	1.273	112.70	0.224
10	261.92	0.194	63.21	0.883	40	113.98	1.829	650.40	0.176
10	90.99	0.552	266.28	0.165	40	77.193	1.382	223.74	1.636
10	393.30	3.452	72.49	0.065	40	242.72	1.692	95.14	0.137
10	65.20	2.117	840.10	2.671	40	746.16	0.017	219.78	0.387
10	106.10	0.041	68.89	2.883	40	130.75	0.050	866.79	1.276
20	71.89	0.582	353.73	0.016	40	17.95	0.225	466.72	1.101
20	96.40	0.007	296.42	1.336	40	110.53	0.154	681.10	0.932
20	20.38	0.932	252.47	0.162	50	226.30	0.975	188.68	3.217
20	639.53	1.473	622.58	0.975	50	95.90	1.098	365.90	6.572
20	804.20	4.775	209.23	0.521	50	885.84	1.452	810.60	2.221
20	405.20	0.765	125.57	0.062	50	85.50	1.392	670.80	9.034
20	252.52	0.117	409.56	1.336	50	217.01	1.166	641.92	0.176
20	593.92	0.154	33.17	2.414	50	220.89	1.673	492.60	0.414
20	154.70	0.168	185.08	4.671	50	837.80	0.032	175.75	1.267
20	77.90	0.057	206.70	0.020	50	20.37	0.564	76.52	9.345
20	102.36	0.226	197.01	0.226	60	19.433	0.417	439.93	3.271
20	754.57	0.378	89.15	1.543	60	359.99	0.033	231.82	0.212
20	931.53	1.287	125.28	1.326	60	123.40	1.284	891.70	0.546
20	71.89	1.338	137.09	2.165	60	17.95	1.521	297.87	0.876
20	568.36	0.178	236.29	0.061	60	643.50	1.087	396.92	1.523
20	489.10	0.721	559.38	0.005	70	156.90	1.264	845.50	0.102
20	722.23	0.882	798.11	5.437	70	339.43	5.117	244.90	0.323
30	973.74	0.179	373.62	2.145	–	–	–	–	–
30	262.33	0.087	257.27	0.976	–	–	–	–	–
30	113.47	0.168	178.84	0.123	–	–	–	–	–

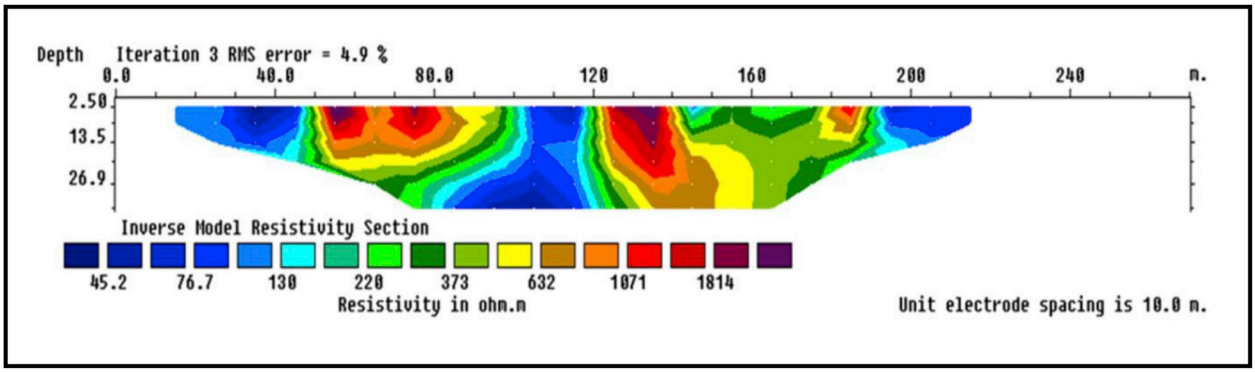

Fig. 9. Sub-surface model of resistivity distribution along Profile 3.

thin overburden rock and accounts for the close proximity of the host formation to the ground surface and, therefore, the shallow depth of the Pb-Zn ores. The boundary between the red and yellow colored areas displayed on the model corresponds to zones of high and low resistivity, and represents the demarcation between the overburden and shale host rock. At the south-western end, the model shows a gradual decrease in resistivity when moving from the ground surface to the base. On this side, the central portion is marked by a contrasting low resistivity zone that is typical of Pb-Zn occurrence (Fig. 13). The resistivity of this area varies between 11.85 and 389.7 Ωm. At the center of the model, a low resistivity signature is continuous from the south-western corner to the north-eastern end portraying the continuity of the disseminated Pb-Zn lodes at a fairly uniform depth as observed in Profiles 2, 4 and 5. The basal portion of the model is dominated by intermediate resistivity signatures that extend to the north-eastern edge.

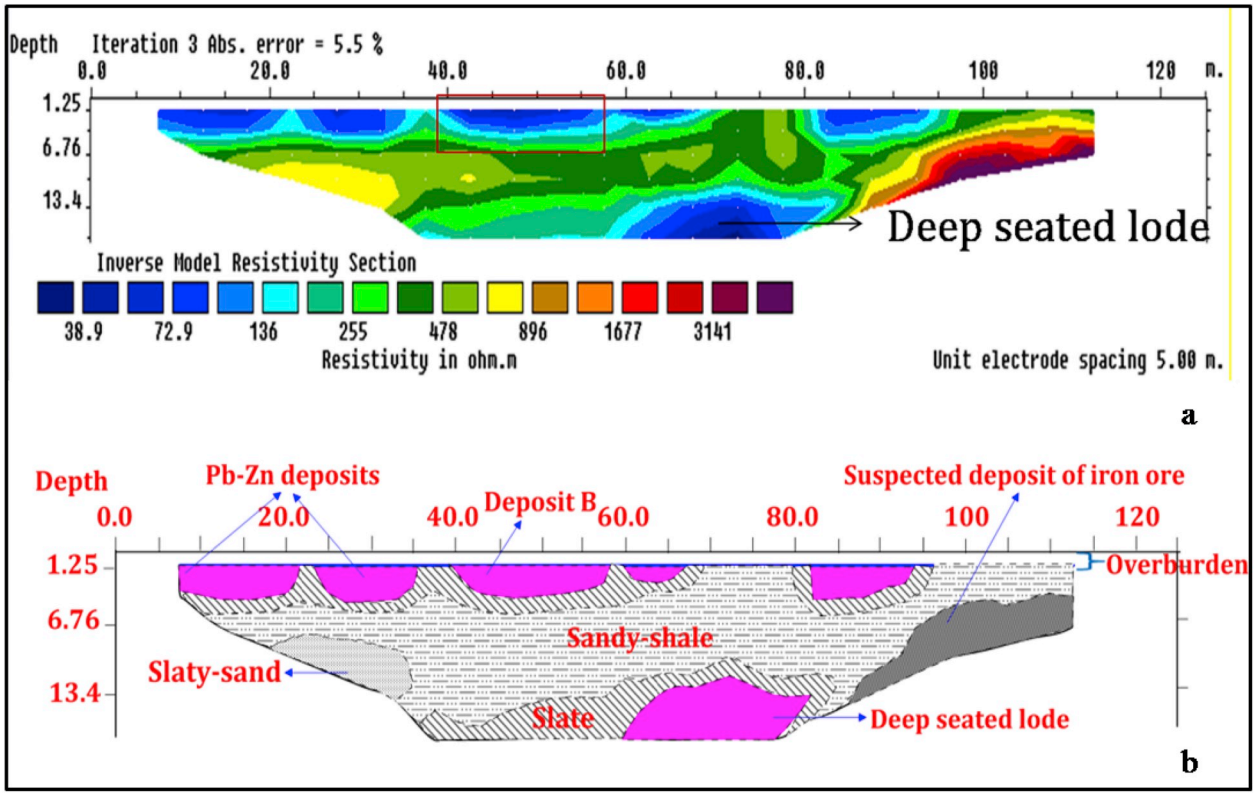

Fig. 10. (a) Sub-surface model of resistivity distribution along Profile 4. DEPOSIT B is enclosed in a square box. (b) Lithologic interpretation of Fig. 10a.

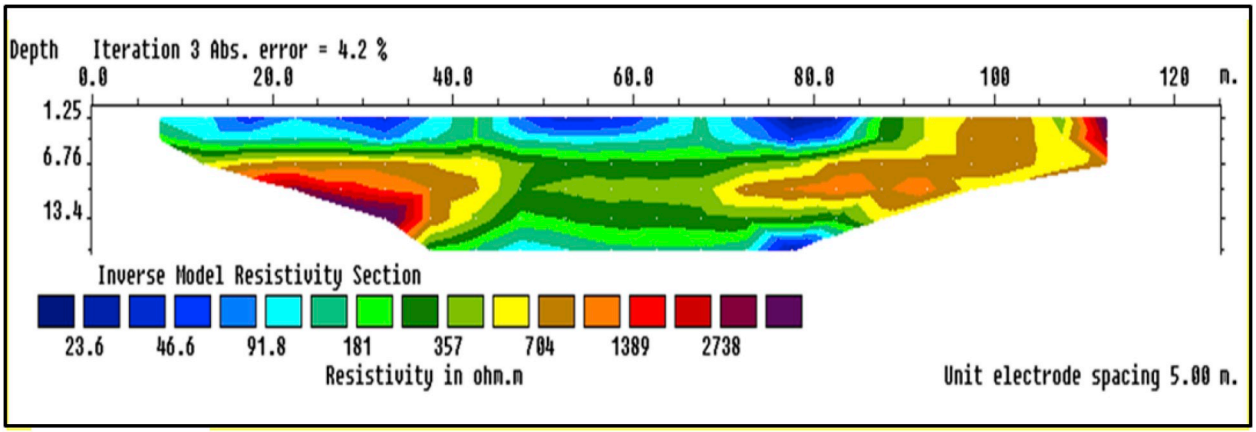

Fig. 11. Sub-surface model of resistivity distribution along Profile 5.

4.3. Limiting depth of target ore bodies inferred from self-potential curves

The resulting self-potential profiles are displayed in Fig. 14(a–e). The shallow depth of the probe (20 m) implies that the results reveal a one layer depth model. Generally, the shallow sources ranged from 5.81 to 2 m, with anomaly values varying from −110 to 237 mV and were characterized by short wavelength signatures. These shallow sources are traceable to vein structures and fractures that are known to harbor mineral ore deposits. Typical SP anomalies exhibit a central negative anomaly and the anomaly minimum is assumed to occur directly over the anomalous body.

In Profile 1, SP anomalies were detected at 30 m and 155 m along the profile (Fig. 14a). The self-potential values recorded decrease gradually from the origin of the graph to about 30 m of the profile line. Beyond this point, the anomaly values were observed to increase up to a distance of about 90 m, after which they decreased substantially and subsequently rose to a value of about 22 mV at a horizontal distance of 165 m. The amplitude of the curve remained fairly uniform beyond this point. The variation in anomaly values along the profile line is attributed to the lateral variation in the electrical properties of the shallow sub-surface rocks. Along this profile, DEPOSIT A was discerned at a depth of 8.3 m between 25 and 35 m of the profile with a central negative anomaly and a half-width (d) of about 10 m (Fig. 14a). The symmetry of the anomaly and the steepness of the slope suggest that the body is spherical in shape.

In profile 4 where DEPOSIT B occurred, four anomalies were delineated with their centres corresponding to 50 m, 100 m, 160 m and 200 m of the profile line (Fig. 14d). The maximum and minimum self-potential anomaly values are 55 and –20 mV, respectively. Along the profile, the measured potential increased slightly from the origin up to a distance of about 15 m after which it abruptly decreased to zero at about 35 m of the profile line. This was followed by a sequence of

Table 3
Resistivity data for Profile 5.

Elect. spacing (m)	Profile 5 Apparent resistivity (Ωm)	Standard deviation	Elect. spacing (m)	Profile 5 Apparent resistivity (Ωm)	Standard deviation
5	178.49	2.514	15	1145.35	2.712
5	167.54	0.167	15	989.38	9.543
5	91.59	0.027	15	52.50	3.421
5	47.81	0.652	15	226.80	4.398
5	90.46	1.763	15	111.91	5.443
5	85.33	2.432	15	239.08	2.167
5	101.77	1.071	15	289.19	2.775
5	97.03	1.991	15	321.65	0.152
5	94.24	0.206	15	127.84	0.226
5	102.51	0.172	15	251.68	1.005
5	95.98	0.122	15	242.91	2.176
5	109.17	0.327	20	492.37	3.217
5	89.44	0.654	20	281.62	1.076
5	88.76	1.832	20	696.76	1.652
5	55.83	1.278	20	284.90	0.165
5	65.80	3.218	20	638.67	2.176
5	36.19	0.142	20	434.04	4.221
5	817.86	0.321	20	362.73	0.195
5	48.92	0.194	20	272.41	0.165
5	61.87	0.327	20	480.97	0.321
10	213.95	0.225	20	183.62	0.652
10	330.23	0.176	20	519.53	0.998
10	414.38	1.453	25	189.72	1.652
10	387.15	0.531	25	261.51	5.014
10	218.14	1.276	25	453.35	2.116
10	786.24	1.423	25	69.71	0.150
10	673.84	1.442	25	70.84	0.003
10	44.61	1.663	25	318.40	0.222
10	90.41	0.162	25	270.68	2.176
10	768.74	2.532	25	247.02	1.005
10	693.30	1.563	30	115.50	2.761
10	750.81	2.673	30	525.06	1.765
10	598.93	1.024	30	902.65	0.532
10	785.05	0.871	30	124.30	0.167
10	691.02	0.427	30	61.32	2.643
10	647.36	0.327	35	225.99	7.002
10	32.96	0.621	35	456.00	0.175
15	773.60	1.67	–	–	–
15	766.28	5.032	–	–	–
15	960.72	7.111	–	–	–

decreases and increases in the anomaly values recorded. Between a distance of 40 m and 55 m of the profile, the anomaly was observed to assume a basin shape with a minimum value of about −18 mV. This symmetrical shape was generated during the movement of the potential electrode over DEPOSIT B (Fig. 13d). The measured anomaly half-width resulting from the presence of this lode is 17 m at an estimated depth of about 14.11 m.

Profile 3 (Fig. 14c) showed three pieces of evidence of mineralization while four anomalies were revealed each by Profile 2 (Figs. 14b) and 5 (Fig. 14e). With the exceptions of Profiles 1 and 2, all potential curves showed a complex variation in anomaly signatures.

4.4. Geo-electric layer model from 1-D VES curves

The underlying stratigraphies for four VES points are displayed graphically in Fig. 15(a–d). All VES curves show close similarity in resistivity signatures but differ in their layer thicknesses, a function of the variation in the thickness of geo-electric layers along the profiles. The similar resistivity trend displayed by all four electro-stratigraphic models is an indication of uniform sub-surface geology beneath the VES stations. Four geo-electric layers were delineated across the transects (Table 4). The four stratigraphic sequences are: overburden, sand-shale heterolith, lead-zinc ores and baked shale. The resistivity range of the thin overburden inferred from the stratigraphic curves is between 508.70 and 745 Ωm. VES 2, 3 and 4 reveal a uniform overburden thickness of approximately 10.3 m, only VES 1 showed a significantly different thickness of 8.0 m. The practically undeviating value in overburden thickness (as well as a fairly uniform elevation) is a clear indication of a flat topography. Additionally, the thinness of the topsoil shows that the deposits are superficial and can be accessed easily using the open cast technique. Beneath the layer of overburden, at slightly shallower depth is a thicker zone of slightly lower resistivity values (177–389 Ωm) consisting predominantly of shales with sand concretions. At much deeper intervals, the models, yet again, show close similarity between signatures by indicating a third localized geo-electric strata of significantly contrasting resistivity compared to the previous layers. This low resistivity zone is an ideal signature indicating lead-zinc occurrence.

VES 1 and 2 were drawn across DEPOSIT A while VES 3 and 4 were traversed across DEPOSIT B. The non-uniform geometry of the ore bodies is clearly demonstrated by the thickness variations between DEPOSITs' A and B as revealed in VES (1 and 2) and VES (3 and 4), respectively. DEPOSIT A showed a slight decrease in thickness from 12.10 m beneath VES 1–11.60 m beneath VES 2 (Fig. 15a and b). Conversely, DEPOSIT B revealed a slight increase in thickness from 9.70 m beneath VES 3–11.30 m beneath VES 4. The average thicknesses of DEPOSITs' A and B inferred from the sounding curves are 11.85 m and 10.50 m, respectively.

4.5. Well core description

Eight wells (AM01, AM02, AM03, AM04, AM05, AM06, AM07 and AM08) were drilled at regularly spaced intervals above DEPOSIT A to a uniform depth of approximately 16 m, at elevations ranging from 57 m to 61 m (Table 5). Drilling information was concentrated along these equispaced wells to produce a fairly systematic data array. Then a geologic interpolation was made for each well and the interpretation was projected in a step-like pattern to the adjoining wells (Fig. 16).

All eight wells intercept the lead-zinc body at varying depths. Generally, the top of the ore body occurs at depths between 13.7 m and 15.2 m (Fig. 16). The depth of the top of the ore body at each well depends on the surface elevation at the well site (Figs. 16 and 17). Results from the core drilling show that the ore zone is directly overlain and underlain by alternating light and dark grey shales that appear fractured and baked (Fig. 17). Above the overlying shale unit is a relatively thin layer of dark grey shales with intercalations of siltstone. Although slightly fractured, this unit of shale is fissile and in some cases consists of sand concretions. This horizon is capped by a layer of sand mixed with clay.

Drilling data acquired for DEPOSIT A (Fig. 18) was used to validate the thickness values obtained from electrical sounding and thus, overcome the non-uniqueness problem of DC resistivity interpretation. Comparing the thickness values of DEPOSIT A which were obtained from the 1D curve and core drill data (Table 5) reveals a very close match. An average ore thickness of 11.85 m inferred from stratigraphic curves (VES 1 and VES 2) compare reasonably well with the mean ore thickness observed from drill cores (11.63 m), suggesting an acceptable degree of confidence as regards the data obtained from vertical electrical drilling.

4.6. Mass, volume and density measurements

The average density value of the samples collected from the two Pb-Zn deposits being studied are presented in Table 6 below.

All eight samples show very high densities, due to the heavy, compact and tightly jammed crystal structure of lead and its high atomic weight. The density values measured for all of the samples equate well with the density range of pure galena (between 7.2 and 7.4 g cm^{-3}) with the exception of samples 1 and 3 of DEPOSIT A (Table 6). The presence of small amounts of other accessory minerals could be

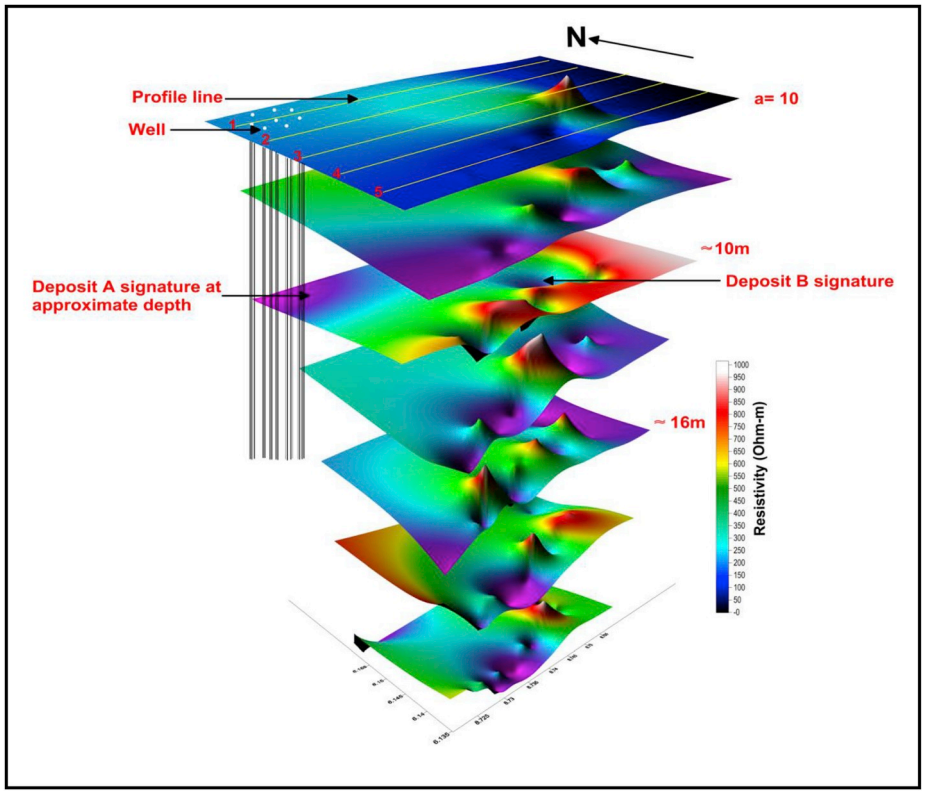

Fig. 12. Resistivity depth slice maps modeled from all five Wenner profiles.

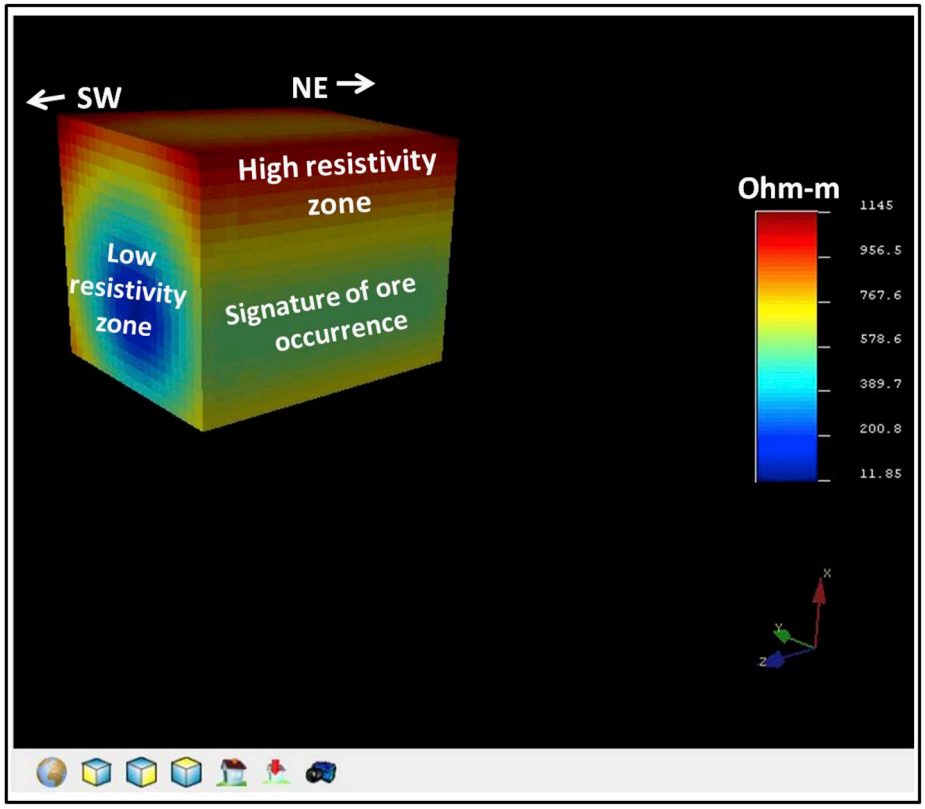

Fig. 13. Variogram based model showing the distribution of apparent resistivity around the survey area.

responsible for the slightly higher values exhibited by these samples. Thus, the density of rock samples is a reflection of their mineral compositions.

The volume of the ore bodies as extracted in Surfer 10.0 environment using the Trapezoidal, Simpson and Simpson 3/8 rules show that DEPOSIT A has a volume of 1201.130 m^3, 1201.129 m^3 and

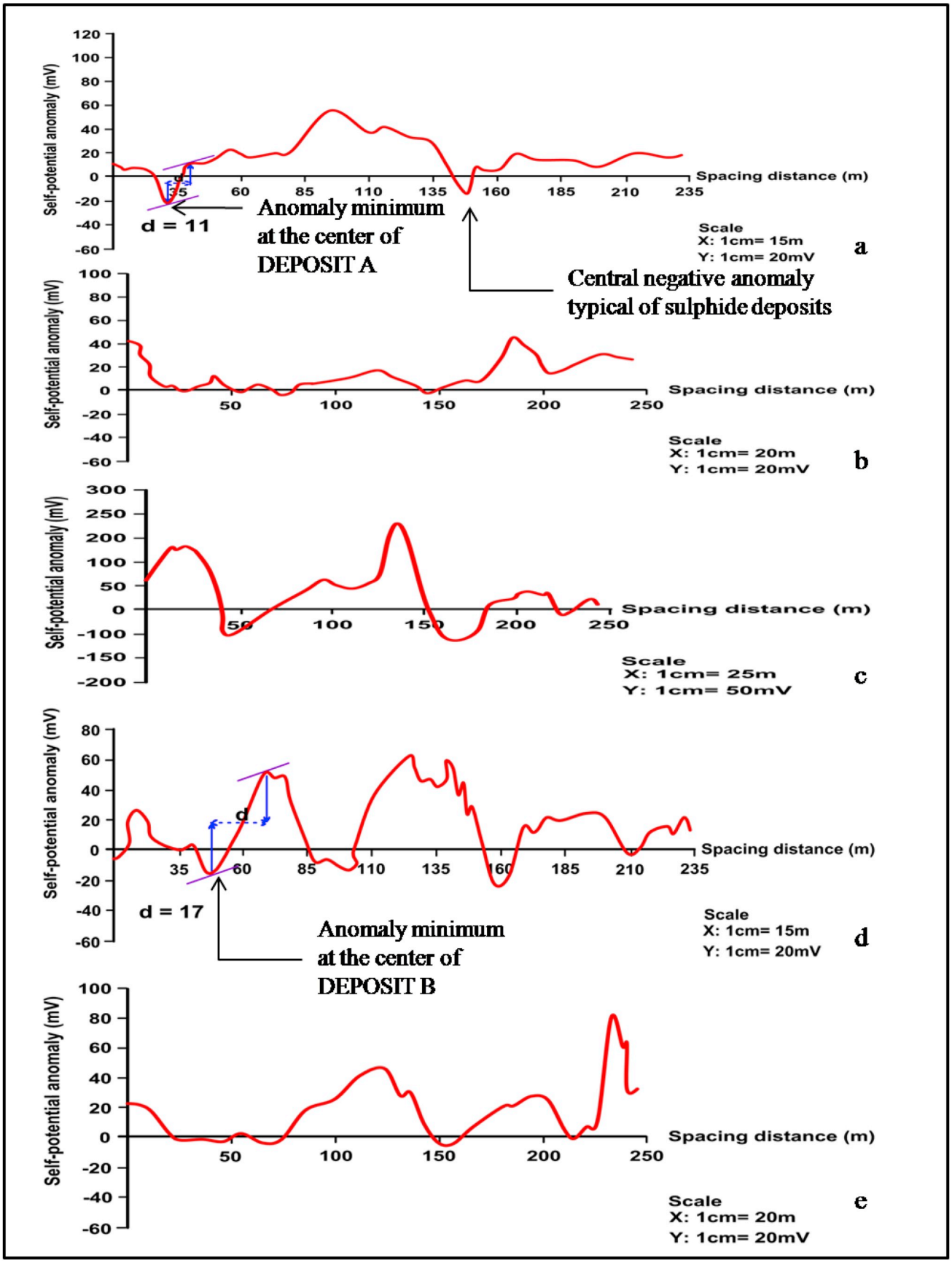

Fig. 14. Self-potential anomaly profiles showing the lateral distribution of natural potential differences along Profiles 1 to 5.

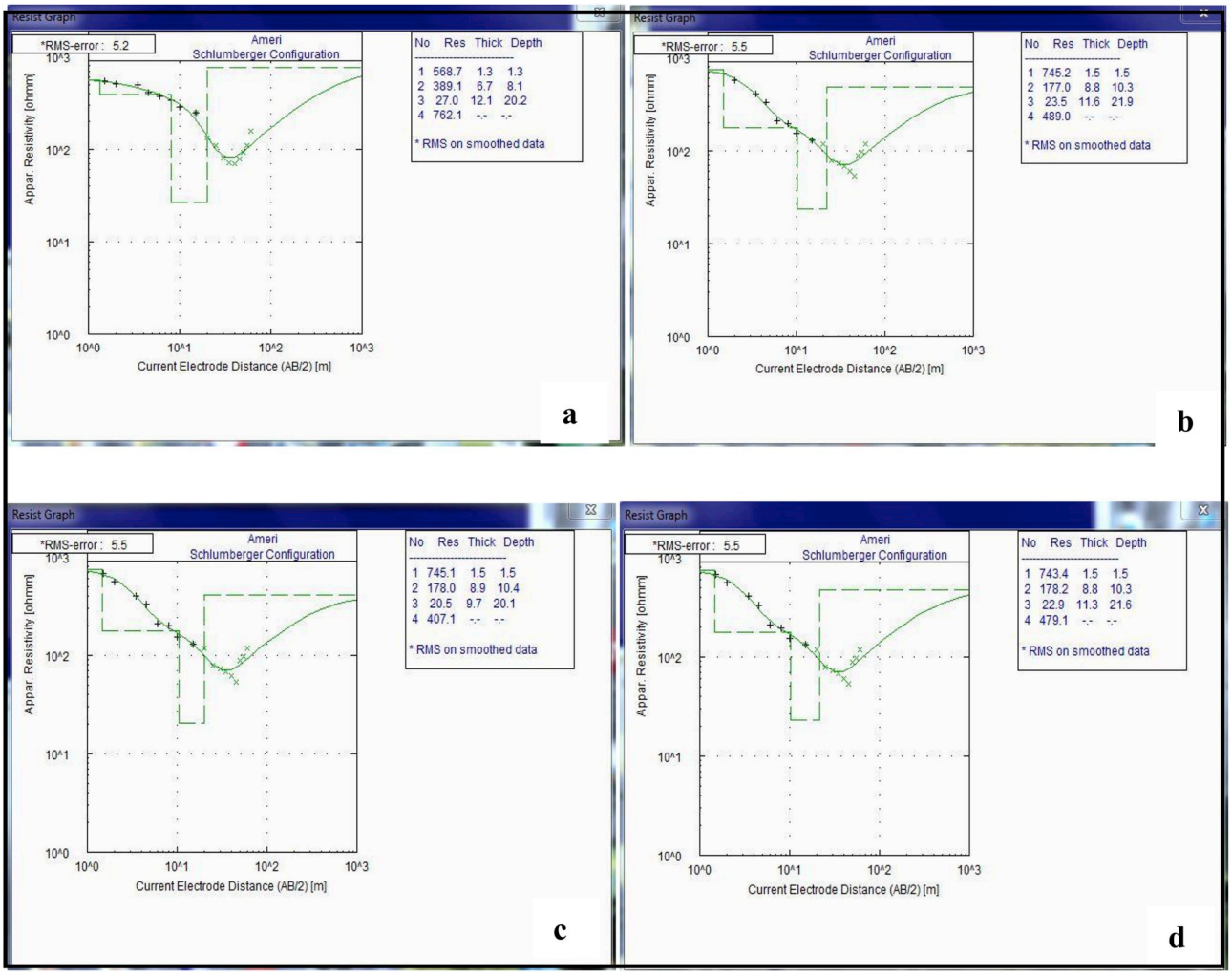

Fig. 15. Geo-electric parameters for (a) VES 1. (b) VES 2. (c) VES 3. (d) VES 4.

Table 4
Stratigraphic parameters from the VES models.

VES location	RMS error	Horizon resistivity (Ωm)				Horizon thickness (m)				Depth to horizon (m)			
		1	2	3	4	1	2	3	4	1	2	3	4
VES 1	5.2	568.7	389.1	27.0	762.1	1.3	6.7	12.1	–	1.3	8.1	20.2	–
VES 2	5.5	745.2	177.0	23.5	489.0	1.5	8.8	11.6	–	1.5	10.3	21.9	–
VES 3	5.5	745.1	178	20.5	407.1	1.5	8.9	9.7	–	1.5	10.4	20.1	–
VES 4	5.5	743.4	178.2	22.9	479.1	1.5	8.8	11.3	–	1.5	10.3	21.6	–

Table 5
Drill-hole data for eight wells above DEPOSIT A.

Field Name: Ameri Report Date: 26/02/2018							
DRILL HOLE SUMMARY							
Drill hole number	Northing	Easting	Elevation (m)	Angle at hole (°)	Angle at ore (°)	True thickness of ore (m)	Thickness error (%)
AM01	6°10′35.69″	8°7′50.63″	60	10	31	11.50	−3.0
AM02	6°10′35.62″	8°7′50.57″	58	12	35	11.00	−1.0
AM03	6°10′35.71″	8°7′50.64″	57	10	32	13.50	−2.0
AM04	6°10′35.63″	8°7′50.60″	61	15	34	12.50	−2.0
AM05	6°10′35.64″	8°7′50.61″	60	17	37	11.50	−2.0
AM06	6°10′35.59″	8°7′50.69″	59	12	35	10.50	−1.0
AM07	6°10′35.53″	8°7′50.65″	59	16	31	11.00	−1.0
AM08	6°10′35.23″	8°7′50.44″	60	17	33	11.50	−1.0

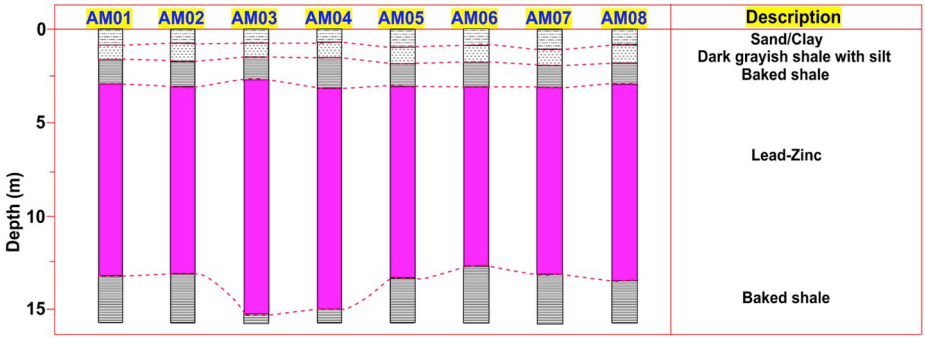

Fig. 16. Correlated stratigraphic logs of well cores.

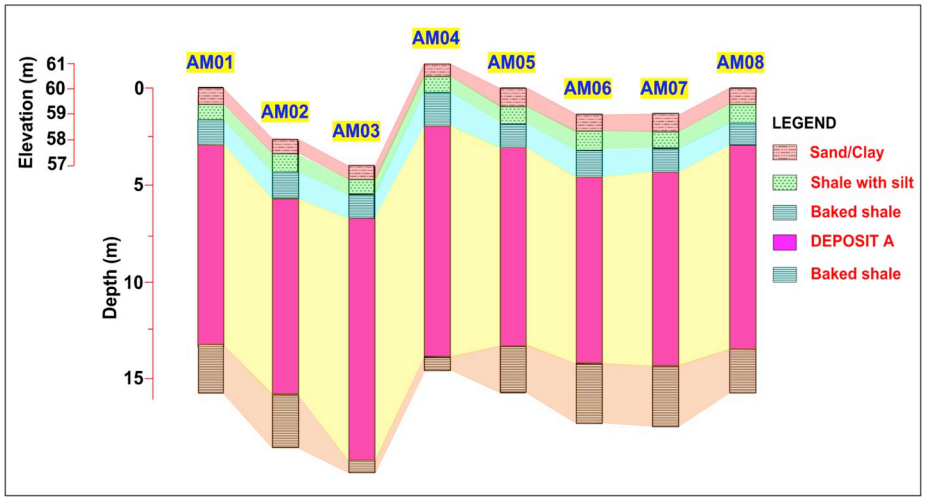

Fig. 17. Correlated stratigraphic logs reflecting the elevation of drilled wells.

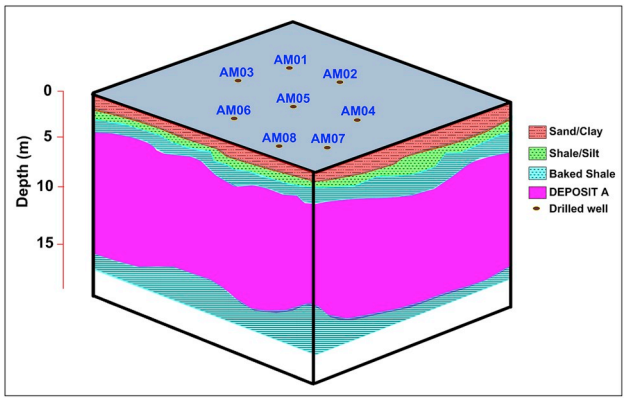

Fig. 18. A stratigraphic sub-surface model showing the locations of wells drilled above DEPOSIT A.

1201.131 m^3, respectively. The Trapezoidal rule volume for LODE B is 347.128 m^3 while the Simpson and Simpson 3/8 rule volumes were 347.130 m^3 and 347.132 m^3 respectively. This suggests that DEPOSIT A has higher dimensions than DEPOSIT B since volume is a function of both thickness and area coverage. It is possible that the size and, therefore, the volume of these deposits were influenced by the dimension of the housing veins.

The volume computation reports computed are shown in Table 7. The accuracy of the volume computations by the three different methods is determined by the difference in the volume calculation of the individual methods. Since the three volume calculations for all the lodes are reasonably similar, the true volume is close to these values. The net volume is therefore reported as the average of the three values.

The average volume for DEPOSITs' A and B is 1201.130 m^3 and 347.130 m^3 respectively.

By applying equation (1), the reserve of DEPOSITs' A and B are obtained and are 8795.97 tonnes and 2524.58 tonnes, respectively. From geometrical analysis, the superior dimension of DEPOSIT A means

Table 6
Density of the Pb-Zn samples.

Sample No.	Deposit A			Deposit B		
	Mass (kg)	Volume (m^3)	Density (kg m^{-3})	Mass (kg)	Volume (m^3)	Density (kg m^{-3})
1	0.0223	0.00000300	7433.33	0.0257	0.00000350	7342.86
2	0.0249	0.00000350	7114.29	0.0183	0.00000250	7320.00
3	0.0260	0.00000350	7428.57	0.0248	0.00000350	7085.71
4	0.0220	0.00000300	7333.33	0.0111	0.00000150	7400.00
Average	0.0238	0.00000325	7323.08	0.0200	0.00000275	7272.72

Table 7
Estimated volume of mineral deposits.

DEPOSIT	Volume (m^3)			Av. Volume (m^3)	Av. Thickness (m)	Area (m)
	Trapezoidal rule	Simpson's rule	Simpson's 3/8 rule			
A	1201.130	1201.129	1201.131	1201.130	11.85	101.361
B	347.128	347.130	347.132	347.130	10.50	33.060

it possesses a greater mass than DEPOSIT B and, as such, is a better prospect.

5. Conclusion

Field geological and geophysical investigations in parts of Ameri reveal the presence of lead-zinc-bearing veins which occur as disseminated metallic deposits in association with other gangue minerals. Two selected lodes with defined geometry, DEPOSIT A and DEPOSIT B, occurring 0.49 km apart in a NW-SE axis are present in shaley host rocks and were quantitatively evaluated. A scalar-geometric approach, involving the arithmetical alliance between the basic variables (area, thickness and density), of ore reserve evaluation was applied for tonnage assessment. Horizontal profiling revealed the deposits to be zones of low resistivity in a background of highly resistive shales. These ore bodies were delineated on graphs of self-potential distribution as areas of negative anomaly measurements. The average thickness values of DEPOSITs A and B inferred from 1D stratigraphic curves are 11.85 m and 10.50 m, respectively. The mean thickness of DEPOSIT A obtained from the VES models was in close agreement with that obtained from drill-hole data. Average densities of representative samples from both lodes compared well with the density of pure galena. DEPOSIT's A and B yielded a tonnage of 8254.37 tonnes and 2706.95 tonnes, respectively. The total estimated reserve of the lodes is 10,778.95 tonnes which is a relatively viable economic quantity and a worthy target for either government or private investment. The shallow depth of occurrence also supports open cast mining which is relatively cost effective. Despite showing fairly good potential in terms of quantity, it is recommended that these deposits be qualitatively accessed to ascertain the exact concentration of lead-zinc in the ores before a final investment decision is made. Additionally, core drilling should be carried out above DEPOSIT B in order to provide a more realistic estimate.

This paper therefore provides evidence of the proven effectiveness of geophysical tools in the detection and predictability of mineral-bearing veins, and also in the detailing and appraisal of the reserves of mineral deposits that lie within them.

Conflicts of interest

None declared.

Ethical statement

Authors state that the research was conducted according to ethical standards.

Funding body

None.

Acknowledgements

The authors gratefully acknowledge Mr. E. Asadu, a technical member of staff of the Department of Geology, University of Nigeria, Nsukka for his role in providing laboratory equipment used for the density determination of the Pb-Zn samples. In addition to providing geophysical equipment (Abem Terrameter and accessories), the management of Chrisgate Hardware Nig. Ltd. also granted permission for the use of their drill hole data. The technical support offered by Mr. Ernest Adibeli during the field exercise is highly appreciated.

References

Adegoke, J. A., & Layade, G. O. (2014). Variation of structural index of Peter's half-slope in determining magnetic source-depth. *Archives of Physics Research, 5*(2), 23–31.
Afolabi, O., Olorunfemi, M. O., Olagunju, A. O., & Afolayan, J. F. (2004). Resource quantification of a kaolin deposit using the electrical resistivity method: Case study from Ikerre-Ekiti, southwest, Nigeria. *Ife Journal of Science, 6*(1), 35–40.
Akande, S. O., & Mucke, A. (1989). Mineralogy, textural and paragenetic studies of the lead-zinc-copper mineralization, Lower Benue Trough and their genetic implications. *Journal of African Earth Sciences, 9*(1), 23–29.
Etim, O. N., Louis, P., & Maurin, J. C. (1988). Interpretation of electrical soundings on the Abakaliki Lead-Zinc and barite prospects, S.E. Nigeria: Geological and genetic implications. *Journal of African Earth Sciences, 7*(5), 743–747.
Ezepue, M. C. (1984). The geologic setting of lead-zinc deposits at Ishiagu, Southeastern Nigeria. *Journal of African Earth Sciences, 2*(2), 97–101.
Farrington, J. L. (1952). A preliminary description of the Nigerian lead zinc field. *Economic Geology, 47*(6), 583–608.
Fatoye, F. B., Ibitomi, M. A., & Omada, J. I. (2014). Lead-zinc-barytes mineralization in the Benue Trough Nigeria: Occurrence and economic prospectivity. *Advances in Applied Science Research, 5*(2), 86–92.
Genik, G. J. (1993). Petroleum geology of cretaceous-tertiary Rift basins in Niger, Chad and Central African Republic. *American Association of Petroleum Geologists Bulletin, 77*(8), 1405–1434.
Grant, N. K. (1971). A compilation of radiometric ages from Nigeria. *Journal of Mining and Geology, 6*, 37–54.
Hoque, M. (1984). Pyroclastics from the lower Benue Trough of Nigeria and their tectonic implications. *Journal of African Earth Sciences, 2*(1), 351–358.
Leach, D. L., Bradley, D. C., Huston, D., Pisarevsky, S. A., Taylor, R. D., & Gardoll, S. J. (2010). Sediment-hosted lead-zinc deposits in earth history. *Economic Geology, 105*(3), 593–625.
Loke, M. H., & Barker, R. D. (1996). Rapid least-squares inversion of apparent resistivity pseudosections by a quasi-Newton method. *Geophysical Prospecting, 44*(1), 131–152.
Lowrie, W. (2007). *Fundamentals of geophysics* (1st ed.). Cambridge: University Press.
Maurin, J. C. (1986). *Analyse de zones decrochantes dans le fosse de la Benoue (Nigeria) et systmatiques U-Pb et Pb-Zn associees.* Ph.D TheseMontpellier: Universite de Montpellier.
Maurin, J. C., Benkhelil, J., & Robineau, B. (1986). Fault rocks of the Kaltungo lineament (NE Nigeria) and their relation with Benue Trough tectonic. *Journal of the Geological Society, 143*(4), 587–599.
Maurin, J., & Lancelot, J. R. (1987). Origines des mineralisations de Pb Zn de la Valle de Benue Nigeria la composition en Pb des galena et de Mineral. *Mineralium Deposita, 2*(2), 99–108.
Monsuro, O. O., Bayewu, O. O., & Oloruntola, M. O. (2011). Application of geophysical and geostatistical method in the estimation of clay deposit reserve of Idofe and environs, southwestern Nigeria. *Mineral Wealth, 160*(1), 41–48.
Mostafijul, M. K., & Farhad, M. H. (2013). Volumetric estimation of coal resources in seam VI for require backfill materials of Barapukuria coal mine, Dinajpur, Bangladesh. *Earth Science, 2*(1), 113–119.
Murat, R. C. (1970). Stratigraphy and paleogeography of the cretaceous and lower tertiary in southern Nigeria. In T. T. Dessauvagie, & A. J. Whiteman (Eds.). *African geology* (pp. 131–158). Ibadan: University Press.
Nwachukwu, S. O. (1972). The tectonic evolution of the southern portion of the Benue Trough. *Geology Magazine, 109*(5), 411–419.
Nwachukwu, S. O. (1975). Temperature of formation of vein minerals in the southern portion of the Benue Trough, Nigeria. *Journal of Geology and Mining, 11*, 45–55.
Obasi, E., Gundu, D. T., Ashwe, A., & Akindele, M. (2015). Determination of work index of Enyigba lead ore, Ebonyi state, south-East Nigeria. *Studies in Engineering and Technology, 2*(1), 103–110.
Obi, D. A., Ekwueme, B. N., & Akpeke, G. B. (2014). Reserve estimation of barite deposits using geological and geophysical investigations in Cross-River state, south-eastern Nigeria. *Journal of Environment and Earth Science, 4*(10), 18–38.
Odeyemi, I. B., Oloruniwo, M. A., & Folami, S. L. (1997). Geological and geophysical characteristics of Ikpeshi marble deposit, Igarra area, southwestern Nigeria. *Journal of Geology and Mining, 33*, 63–79.
Offodile, M. E. (1976). A review of the geology of the cretaceous of the Benue valley. In C. A. Kogbe (Ed.). *Geology of Nigeria* (pp. 201–245). Lagos: Elizabethan Publication Company.

Offodile, M. E., & Reyment, R. A. (1976). *Stratigraphy of the Keana-Awe area of the middle Benue region of Nigeria. Vol. 7*. Bulletin of the Geological Institute of the University of Uppsalla.
Oha, I. A., Mosto, K. M., & Dada, S. S. (2017). Contrasting styles of lead-zinc-barium mineralization in the lower Benue Trough, southeastern Nigeria. *Earth Sciences Research Journal, 21*(1), 7–16.
Ojoh, K. A. (1992). The southern part of the Benue Trough (Nigeria) Cretaceous stratigraphy, basin analysis, paleo-oceanography and geodynamic evolution in the Equatorial Domain of the South Atlantic. *Nigerian Association of Petroleum Explorationists Buletin, 7*, 131–152.
Olade, M. A. (1976). On the genesis of lead-zinc deposits in Nigeria Benue rift (aulacogen) a re-interpretation. *Journal of Geology and Mining, 13*, 20–27.
Olade, M. A., & Morton, R. D. (1985). Origin of lead-zinc mineralization in the southern Benue Trough, Nigeria: Fluid inclusion and trace element studies. *Mineralium Deposita, 20*(2), 76–80.
Onimisi, M., Abaa, S. I., Obaje, N. G., & Sule, V. I. (2015). A preliminary estimate of the reserve of the marble deposit in Itobe area, central Nigeria. *Journal of Geology and Geophysics, 4*(1), 1–11.
Orajaka, I. P. (1965). Geology of Enyigba, Ameri and Ameka lead-zinc mines. *The Journal of Geology, 3*, 49–59.
Ramazi, H., & Mostafaie, K. (2013). Application of integrated geoelectrical methods in Marand (Iran) manganese deposit exploration. *Arabian Journal of Geosciences, 6*(8), 2961–2970.
Reyment, R. A. (1965). *Aspect of the geology of Nigeria* (1st ed.). Ibadan: University Press.
Rolo, R. M., Radtke, R., & Costa, J. F. (2017). Signed distance function implicit geologic modeling. *International Engineering Journal, 70*(2), 221–229.
Simpson, A. (1954). The Nigerian Coalfield: The geology of parts of Owerri and Benue provinces. *Bulletin – Geological Survey of Nigeria, 24*, 1–85.
Sinclair, A. J., & Blackwell, G. H. (2002). *Applied mineral inventory estimation* (1st ed.). Cambridge: University Press.
Soulaimani, S., Manar, A., Chakiri, S., Alloiza, M., Ezzayani, J., El-Hmidi, F., et al. (2017). 3D modeling and reserve estimation using gravity data of Hajjar central ore body (Marrakech region, Morocco). *Bulletin de l'Institut Scientifique, 39*, 25–34.
Tercan, A. E., Unver, B., Hindistan, M. A., Ertunc, G., Atalay, F., Unal, S., et al. (2012). Seam modeling and resource estimation in the coalfields of western Anatolia. *International Journal of Coal Geology, 112*, 94–106.
Wang, Q., Deng, J., Liu, H., Yang, L., Wan, L., & Zhang, R. (2010). Fractal models for ore reserve estimation. *Ore Geology Reviews, 37*, 2–14.